VYSOKÉ UČENÍ TECHNICKÉ V BRNĚ
BRNO UNIVERSITY OF TECHNOLOGY

FAKULTA STROJNÍHO INŽENÝRSTVÍ
ÚSTAV FYZIKÁLNÍHO INŽENÝRSTVÍ

FACULTY OF MECHANICAL ENGINEERING
INSTITUTE OF PHYSICAL ENGINEERING

OPTICAL SETUP FOR TORQUE DETECTED ELECTRON SPIN RESONANCE SPECTROSCOPY

DIPLOMOVÁ PRÁCE
MASTER'S THESIS

AUTOR PRÁCE
AUTHOR

Bc. MICHAL KERN

BRNO 2015

VYSOKÉ UČENÍ TECHNICKÉ V BRNĚ

BRNO UNIVERSITY OF TECHNOLOGY

FAKULTA STROJNÍHO INŽENÝRSTVÍ
ÚSTAV FYZIKÁLNÍHO INŽENÝRSTVÍ

FACULTY OF MECHANICAL ENGINEERING
INSTITUTE OF PHYSICAL ENGINEERING

OPTICAL SETUP FOR TORQUE DETECTED ELECTRON SPIN RESONANCE SPECTROSCOPY

OPTICKÝ SYSTÉM PRO TORZNĚ DETEKOVANOU ELEKTRONOVOU SPINOVOU REZONANČNÍ SPEKTROSKOPII

DIPLOMOVÁ PRÁCE
MASTER'S THESIS

AUTOR PRÁCE — Bc. MICHAL KERN
AUTHOR

VEDOUCÍ PRÁCE — Ing. PETR NEUGEBAUER
SUPERVISOR

BRNO 2015

Vysoké učení technické v Brně, Fakulta strojního inženýrství

Ústav fyzikálního inženýrství
Akademický rok: 2014/2015

ZADÁNÍ DIPLOMOVÉ PRÁCE

student(ka): Bc. Michal Kern

který/která studuje v **magisterském navazujícím studijním programu**

obor: **Fyzikální inženýrství a nanotechnologie (3901T043)**

Ředitel ústavu Vám v souladu se zákonem č.111/1998 o vysokých školách a se Studijním a zkušebním řádem VUT v Brně určuje následující téma diplomové práce:

Optický systém pro torzně detekovanou elektronovou spinovou rezonanční spektroskopii

v anglickém jazyce:

Optical setup for torque detected electron spin resonance spectroscopy

Stručná charakteristika problematiky úkolu:

Torzně detekovaná elektronová spinová rezonance (TDESR), vyvíjená na Štuttgartské univerzitě, je širokospektrální spektroskopická technika na studium elektronové struktury vzorků s omezeným počtem spinů u vysokých frekvencích (THz). Základem TDESR je torzní magnetometrie, při které je magnetizace vzorku studována pomocí torze, kterou působí na ohebné raménko ve statickém magnetickém poli. Ozařováním vzorku mikrovlnou se dosáhne ESR, což způsobí změnu magnetizace, která je měřitelná sledováním ohybu raménka. Aktuální experimentální sestava používá kapacitní můstek k měření kapacity mezi raménkem a nehybnou deskou. Cílem této diplomové práce je navrhnout, implementovat a odzkoušet optický systém pro spektroskop TDESR, který nahradí aktuální kapacitní detekci a měl by vést ke zvýšení citlivosti sestavy.

Cíle diplomové práce:

Počáteční testování a získání předběžných výsledků optické sestavy proběhne na Ústavu fyzikálního inženýrství na VUT v Brně. Následně se sestava přemístí na Ústav fyzikální chemie Štuttgartské univerzity, kde proběhne implementace do spektrometru, finalizace a testovací měření na látkách se známým ESR spektrem.

ABSTRACT

This thesis has been devoted to the improvement of a Torque Detected Electron Spin Resonance (TDESR) spectrometer by replacing the current capacitive detection of cantilever bending with optical methods. The thesis covers the basics of Electron Spin Resonance (ESR) spectrometry with the focus on TDESR and the field of single molecule magnetism. Laser beam deflection and interferometric detection methods are explained. The design of the TDESR spectrometer and its performance is shown on successfully obtained high quality TDESR spectra of an Fe_4 single molecule magnet single crystal. Obtained results prove the feasibility of implemented detection method and its superiority with respect to the previously used capacitive method in terms of quality, resolution and speed. To further improve the TDESR setup, we have designed and assembled a system which uses an interferometer for detection of cantilever bending.

KEYWORDS

torque detected electron spin resonance, spectroscopy, single molecule magnet, laser beam deflection, interferometer

ABSTRAKT

Táto diplomová práca sa venuje vylepšeniu spektroskopu Torzne Detegovanej Elektrónovej Spinovej Rezonancie (TDESR) výmenou aktuálnej kapacitnej detekcie výchylky ohybného ramienka za optické metódy. Práca popisuje základy Elektrónovej Spinovej Rezonančnej (ESR) spektroskopie s dôrazom na TDESR a tému magnetizmu jednomolekulových magnetov. Následne je vysvetlená detekcia výchylky ramienka pomocou odrazu laserového zväzku a interferometrie. Všetky kroky nutné k skonštruovaniu spektrometra a jeho uvedenia do prevádzky sú podrobne popísané. Pomocou detekcie odrazu laserového zväzku sme úspešne získali vysoko kvalitné TDESR spektrá kryštálu jednomolekulového magnetu Fe_4. Týmto meraním sme dokázali vhodnosť použitia tejto metódy a jej výraznú prevahu nad pôvodnou kapacitnou detekciou, najmä v oblasti kvality, rozlíšenia a rýchlosti. Zároveň sme na ďalšie vylepšenie TDESR spektrometra navrhli a zostrojili zostavu využívajúcu na detekciu výchylky interferometer.

KLÍČOVÁ SLOVA

torzne detekovaná elektrónová spinová rezonancia, spektroskopia, jednomolekulové magnety, odraz laserového zväzku, interferometer

KERN, Michal *Optical setup for torque detected electron spin resonance spectroscopy*: master's thesis. Brno: Brno University of Technology, Faculty of Mechanical Engineering, Institute of Physical Engineering, 2015. 65 p. Supervised by Dr. Ing. Petr Neugebauer,

DECLARATION

I declare that I have written my master's thesis on the theme of "Optical setup for torque detected electron spin resonance spectroscopy" independently, under the guidance of the master's thesis supervisor and using the technical literature and other sources of information which are all quoted in the thesis and detailed in the list of literature at the end of the thesis.

As the author of the master's thesis I furthermore declare that, as regards the creation of this master's thesis, I have not infringed any copyright. In particular, I have not unlawfully encroached on anyone's personal and/or ownership rights and I am fully aware of the consequences in the case of breaking Regulation § 11 and the following of the Copyright Act No 121/2000 Sb., and of the rights related to intellectual property right and changes in some Acts (Intellectual Property Act) and formulated in later regulations, inclusive of the possible consequences resulting from the provisions of Criminal Act No 40/2009 Sb., Section 2, Head VI, Part 4.

Brno ....

(author's signature)

ACKNOWLEDGEMENT

There are many people who contributed to this work, or just helped me to go through my studies - I can consider myself very lucky that I have met such a number of talented and friendly people everywhere life has taken me.
I am very grateful to my supervisor, Dr. Ing. Petr Neugebauer, for introducing me to the field of electron spin resonance, his friendly advice, encouragement and freedom to work independently, to prof. Joris van Slageren, for the opportunity to work in his group on such interesting topics, for sharing his expertise and the help with this thesis, to María Dörfel for showing me the way around the spectrometer, how to handle single crystals and willingness to help, to Dalibor Šulc for bringing his interferometer to Stuttgart, profilometry measurements and great collaboration, to Raphael Marx for his invaluable support during measurements and sharing with me the breakthrough moments, Dominik Bloos for his incredible programming skills and fruitful discussions, Jan Vaverka and Heiko Bamberger for short, but diligent taking care of my cryogenic liquids and the whole van Slageren workgroup for a warm welcome and great working atmosphere. I must also thank to Eric Heintze and Marian Blankenhorn from 1. Physical Institute of University of Stuttgart, for readily sharing their expertise and the first polished cantilever, without which the work would be quite delayed, to PD Dr. Benedetta Casu and Dr. Francesca Ciccullo from University of Tübingen for the XPS and AFM measurements on cantilevers, and to my dear friends in Brno, Lukáš Flajšman for his help with first measurements, Marek Vaňatka for NiFe depositions and Lukáš Kormoš for electron beam lithography.
I must express my gratitude to Veronika Vaškebová for her love and constant support. And last but not least, I thank my family, my sister and both of my parents, without whom none of this would be possible.

Brno ....

(author's signature)

MOTIVATION

The Torque Detected Electron Spin Resonance (TDESR) technique was developed at the University of Stuttgart in 2010 by Fadi El Hallak, Joris van Slageren and Martin Dressel to investigate anisotropic paramagnetic samples. In this method the Electron Spin Resonance (ESR) spectrum of a magnetically anisotropic sample (single crystal, thin film, etc.) is obtained by measuring its magnetization while simultaneously irradiating it with Microwave (MW) radiation. This thesis is a continuation of the previous work on improving this technique and involves implementation of new detection methods of cantilever deflection detection. The aim of this work is not to achieve the ultimate sensitivity of a single spin, which was already achieved, but rather to perfect the TDESR technique to a point, where it will be suitable for investigation of surfaces covered with thin layers of magnetic molecules. Such molecular assemblies prove suitable for the future of data storage or quantum computing. For real-life applications, however, the behaviour of these molecules has to be investigated at reasonable scale, which is why instead of an Atomic Force Microscope (AFM) microcantilever, we use a cantilever with a macroscopic sample area.

CONTENTS

List of Abbreviations

ESR	Electron Spin Resonance
TDESR	Torque Detected Electron Spin Resonance
SMM	Single Molecule Magnet
RADAR	RAdio Detection And Ranging
NMR	Nuclear Magnetic Resonance
cw	continuous wave
MW	Microwave
RF	Radio Frequency
FDMR	Frequency Domain Magnetic Resonance
HS	Hyperfine Splitting
MRFM	Magnetic Resonance Force Microscopy
SQUID	Superconducting QUantum Interference Device
CTM	Cantilever Torque Magnetometry
BWO	Backward-Wave Oscillator
QO	Quasi-Optical
ZFS	Zero-Field Splitting
ESEEM	Electron Spin Echo Envelope Modulation
PELDOR	Pulsed ELectron DOuble Resonance
HYSCORE	HYperfine Sublevel CORrElation spectroscopy
WWII	World War II
QTM	Quantum Tunnelling of Magnetisation
AFM	Atomic Force Microscope
FEA	Finite Element Analysis
PSD	Position Sensitive Detector
VTI	Variable Temperature Insert

1 INTRODUCTION

This chapter will introduce the reader to the technique of ESR and TDESR. We will go from the discovery of magnetic resonance to the more advanced techniques used today with a focus on TDESR. After briefly discussing the theoretical background of our measurements, a general ESR spectrometer will be described. The performance of our setup was tested on Single Molecule Magnets (SMMs), therefore they will be shortly introduced in the last section as well.

1.1 Historical perspective

ESR spectroscopy, sometimes equivalently called Electron Paramagnetic Resonance (EPR) spectroscopy, may be thought of as an extension of the revolutionary experiment performed by Stern and Gerlach in the 1920s [1]. In this one of the most fundamental experiments of modern physics they proved that, despite the sphericity of the atom, the magnetic moment of the electron can have only discrete orientations. Around 1936, by continuation of their experiment, Rabi observed the phenomenon of what is today known as Nuclear Magnetic Resonance (NMR) in molecular beams[1]. Inspired by his results, Zavoisky, a researcher from Kazan, started to work in the field of magnetic resonance. He likely observed NMR in liquids and solids first, but he didn't have a sufficiently homogeneous magnetic field and discarded the results as unreproducible [2]. After that he focused on electron spin resonance which doesn't require such field homogeneity, but very sensitive detection equipment instead. Officially, he observed the phenomenon of ESR for the first time in 1944 via MW absorption in a salt sample, at a magnetic field of 4.76 mT for a frequency of 133 MHz. However, he likely observed ESR even sooner, but due to his life circumstances in Tatarstan, isolated from the western world during World War II (WWII), his achievements stayed unrecognised until a year after his death[2] [3]. In the western world, NMR in liquids was achieved by Bloch and Purcell in 1946, for which they shared a Nobel Prize in Physics in 1952.

During WWII, the RADAR[3] technology was developed and used mainly in a then-secret frequency band called, for safety reasons, X-band. Frequencies in the region of 8-12 GHz were used since they have low atmospheric absorption. After 1946, the ESR technique was rapidly exploited and refined, mainly because of the availability of equipment in this MW region [4]. Electron transitions correspond to

[1] Resulting in a Nobel prize in Physics in 1944.

[2] In 1977 his discovery of EPR was acknowledged by the International EPR Society.

[3] Although now most of the time used as a regular word, it stands for RAdio Detection And Ranging.

the GHz range, which is in contrast with NMR, where MHz frequencies are used - a reason that lies behind the slower advancement of ESR compared with NMR. Although this transition to the X-band range significantly improved the resolving power of ESR (compared to the first experiments of Zavoisky), the need for even higher frequencies to improve the sensitivity and resolution of ESR spectrometers was soon recognized (one reason for that can be seen in Fig. 1.1). The technological problem of higher frequencies wasn't to be solved until the 1970s, when the group of Lebedev implemented a 148 GHz spectrometer [5]. Since then the frequencies steadily climbed (Lynch [6], Muller [7]) and nowadays spectra at 700 GHz [8] and over 1 THz are routinely recorded [9]. A significant step was also the start of using Quasi-Optical (QO) techniques [6][10], which are used nowadays in most laboratories.

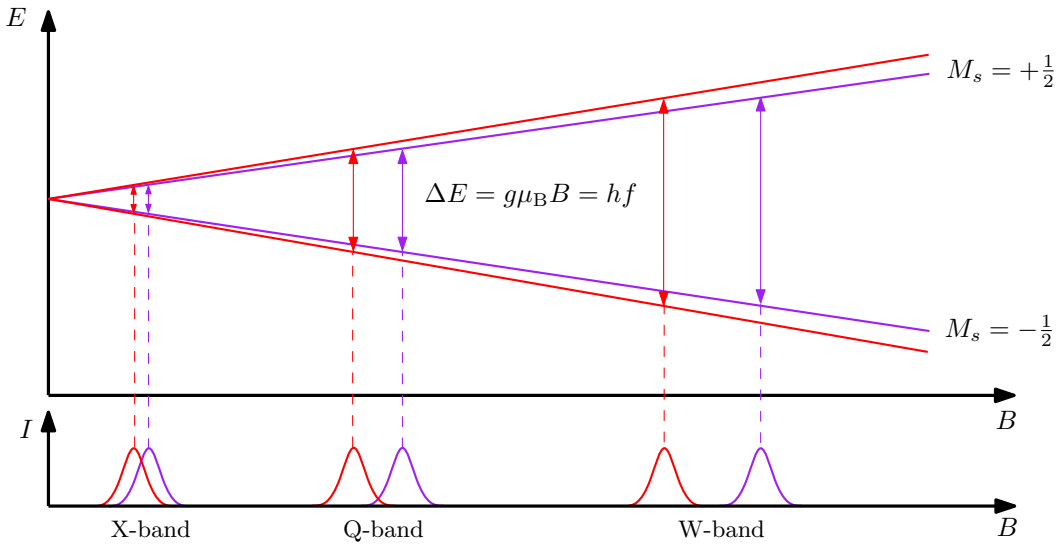

Fig. 1.1: A simplified energy level diagram of spin $S = 1/2$ system with 2 species with different g values (system characteristic constants defined in section 1.2). In the X-band frequency range, they are almost indistinguishable. By increasing the magnetic field and frequency, we get greater separation of the energy levels and we can identify the species at Q-band (33-50 GHz). However, at W-band (75-110 GHz) they are completely separated and we can see all of their features.

Up until the 1950s both magnetic resonance techniques were used with continuous wave (cw) irradiation. After the first experiments with Radio Frequency (RF, MHz region) pulses by Hahn [11], the true potential of NMR was discovered and today NMR is carried out almost solely in pulsed operation. For ESR it took almost twenty additional years to successfully operate in the pulsed regime. The problem is creating sufficiently short high frequency (MW region, GHz) pulses and detecting fast transitions, typically three orders of magnitude faster than in NMR. Due to this fact it took longer for pulsed ESR to flourish, but with the advances in MW generation and detection, combined with computers, there is now a plethora

of sophisticated pulsed experiments which have become routine with commercially available ESR spectrometers[4] [5].

In all mentioned experiments, ESR was detected through MW absorption, i.e., a drop in the intensity of radiation transmitted through or reflected from a sample. This method is still used in most setups, but it isn't without problems. Due to the limited energy per photon, detection of MWs is inherently insensitive, which limits the ultimate sensitivity of this technique. Commercial instruments are typically able to detect up to 10^8 spins per Gauss linewidth - with use of surface microresonators it can be pushed as low as 10^4 spins per Gauss [12]. However, the ultimate sensitivity is of course the detection of a single spin, which could not be achieved with a conventional ESR spectrometer. This was achieved by a variety of other detection mechanisms, for example electrical [13] or by direct detection of the magnetic moment [14].

In 1992 it was proposed by Sidles and experimentally proven by Rugar that magnetic resonance can be measured mechanically via a microcantilever in an AFM [15]. They detected a change in the microcantilever's eigenfrequency due to a change in force acting upon the sample in a magnetic field gradient. Single spin sensitivity of this method was achieved also by Rugar in 2004 [14] (see Fig.1.2).

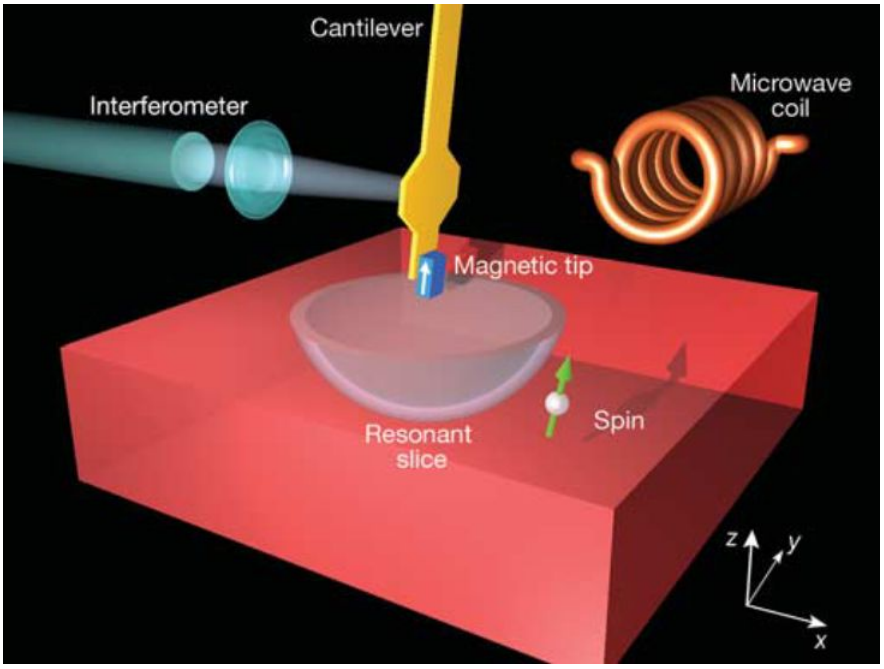

Fig. 1.2: Configuration of the single spin experiment based on magnetic resonance force microscopy by Rugar. Picture taken from [14].

[4]For the interested reader we can mention for example ESEEM, HYSCORE or PELDOR. Since they are not the subject of our study, we will not explain them, but they can be found in relevant literature, for example in [4].

In 2006, Ohta successfully expanded this method and created a highly sensitive pulsed ESR spectrometer, measuring at liquid helium temperatures, using a commercial AFM microcantilever [16]. They have estabilished that the measured ESR signal was due to torque arising from the g tensor anisotropy in a homogeneous magnetic field. Ohta and Ohmichi still continue to develop this method by implementing higher magnetic fields and different MW sources [17][18][9].

A different road was taken at the University of Stuttgart by van Slageren, El Hallak and Dressel, where instead of using a microcantilever, they developed a macrocantilever [19] (see Fig. 1.3). By capacitively detecting deflection of the cantilever while irradiating the sample on the cantilever with MWs, they recorded broadband ESR spectra and named this technique torque detected electron spin resonance. This thesis is a continuation of their previous work.

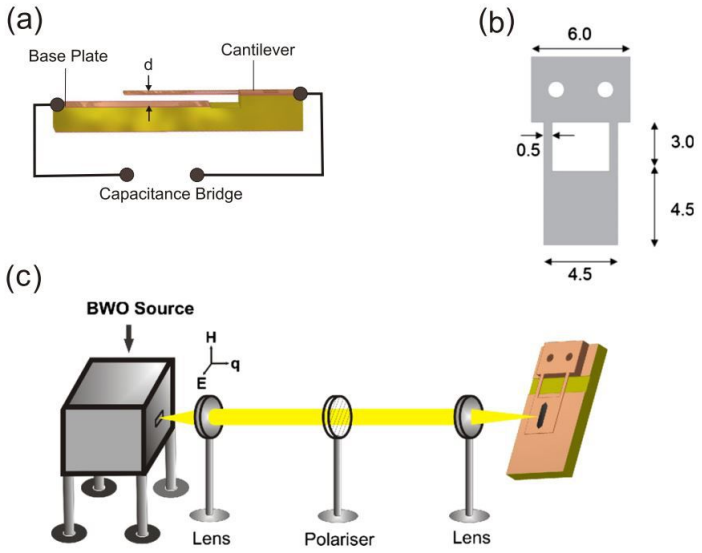

Fig. 1.3: Experimental configuration of the TDESR setup developed by El Hallak, van Slageren and Dressel in Stuttgart. (a) Torque meter with the cantilever placed at a distance d from the base plate, (b) cantilever, with dimensions in milimeters, (c) the quasioptical setup which illustrates how the beam is focused onto the sample placed on the cantilever. Picture taken from [19].

1.2 Electron spin resonance

The phenomenon of ESR is most easily understood on the simplest system of hydrogen atom with one unpaired electron, therefore a total spin of $S = 1/2$. A simple energy level diagram of such system can be seen on Fig. 1.1. Without a magnetic field present, this system has two degenerate eigenstates ($M_S = \pm 1/2$). The introduction of a nonzero external magnetic field B lifts the degeneracy, therefore

energetically separates the eigenstates. The energy separation of these two states is given by the equation:

$$\Delta E = hf = g\mu_{\mathrm{B}}B, \tag{1.1}$$

where h is the Planck constant, f is the frequency of an incoming photon, g is the Landé g-factor, μ_{B} is the Bohr magneton and B is the external magnetic field. If we apply electromagnetic radiation with its magnetic field oscillating perpendicular to the external field B with frequency f, resonance absorption will occur. To observe this phenomenon, however, a population difference between the two states is also necessary.

In order to perform an ESR experiment, we can choose to either irradiate the sample with a MW with constant frequency and sweep the magnetic field (field domain, conventional method) or hold the magnetic field static and sweep with the frequency (frequency domain, called Frequency Domain Magnetic Resonance (FDMR)). Since the samples in usual ESR spectrometers are placed in a resonant cavity optimized for one MW frequency, most experiments are done in the field domain. It is also far less technologically challenging to sweep magnetic fields while irradiating with constant MW frequency. However, the frequency sweep option is more convenient, since frequencies can be swept much faster than magnetic fields and in this configuration we look directly on the energy spectrum, without the need to recalculate it. Nowadays, thanks to the technological progress, stable MW sources that allow frequency sweeping are also available and FDMR experiments are becoming more common.

Typical spectra from both techniques can be seen on Fig.1.4. As we can see, the spectra are mirrored - reason for this is that if we perform the experiment in the field domain, i.e. we keep the irradiation frequency constant and we sweep with the magnetic field, high energy transitions are observed first, whereas if we move in the frequency domain, we are set at one magnetic field and we are increasing the energy of MW radiation - therefore we see lower energy transitions first.

1.3 Electron spin resonance detected via change in magnetization

The notion of detecting ESR via change in magnetization is not recent one - the first experiment of this kind was done by Candela in 1965 [20]. Instruments at that time were basically very elaborate balances. By placing a homogeneous sample of volume V (the needed amount was usually in the gram range, which is compared to current sensitivities a large amount) into a magnetic field B (oriented for example

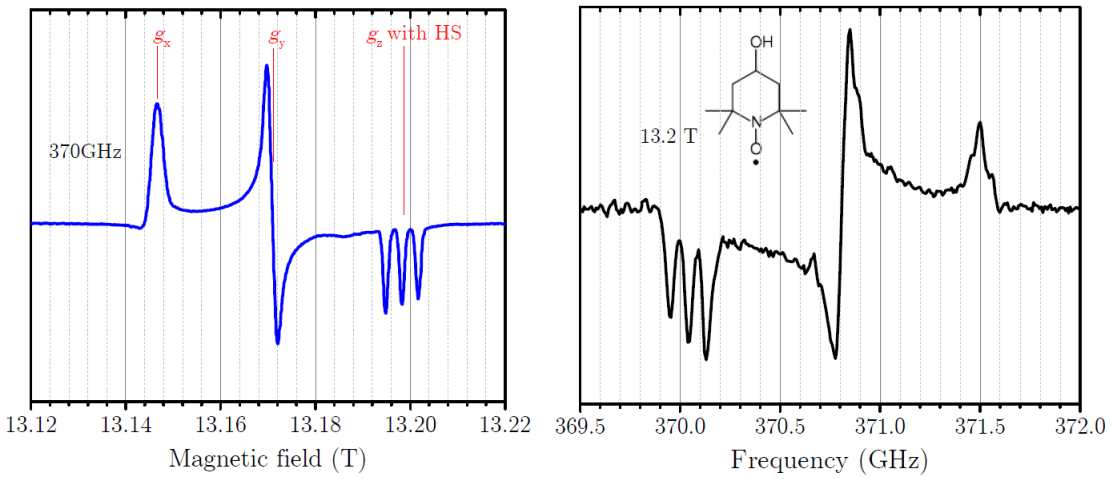

Fig. 1.4: Comparison of ESR (recorded at 370 GHz) and FDMR (recorded at 13.2 T) spectra. The sample was the TEMPO nitroxide radical, which displays both g value anisotropy and Hyperfine Splitting (HS) due to the interaction between the electron and nitrogen nucleus (with nuclear spin $I = 1$). The g value anisotropy can be readily distinguished at sufficiently high frequencies. Both of these spectra were recorded at the high field ESR spectrometer at the University of Stuttgart by Dr. Ing. Neugebauer.

along the x direction) it experienced a force of

$$F_x = \frac{(\chi - \chi_{\mathrm{M}})}{2\Gamma_{\mathrm{m}}} \int_V \frac{\mathrm{d}B^2}{\mathrm{d}x} \mathrm{d}V, \tag{1.2}$$

where χ is the field independent isotropic magnetic susceptibility, χ_{M} is the susceptibility of the medium and Γ_{m} is the magnetic constant [21]. This force can enhance or counter the sample weight and, by a series of measurements, the absolute susceptibility of the sample was obtained. In a sophisticated experiment, Candela implemented into this technique MW radiation and measured the influence of electron spin resonance on the susceptibility. Since then magnetometry has advanced and today there are various magnetometric methods combined with ESR spectroscopy, such as Superconducting QUantum Interference Devices (SQUIDs) [22], micro-SQUIDs [23], cantilever magnetometry [16][15] and Hall probes [24]. In our work we have chosen Cantilever Torque Magnetometry (CTM) to be ideal for our purposes and the available setup, since SQUIDs and micro-SQUIDs are very sensitive but have a relatively slow response time and have a upper magnetic field limit around 8 T (even lower for micro-SQUID), and though Hall bars are sensitive enough and have fast response times, they have shown heating effects under MW irradiation [24].

1.3.1 Cantilever torque magnetometry

Earlier versions of torque meters were based on the torsion pendulum developed more than fifty years ago [25] - since then much progress has been made to render this technique simpler and more sensitive. The pioneering work of Griessen [26], who developed a capacitance torque meter, inspired many groups to use flexible beams with one end fixed (i.e., cantilevers) to form a parallel-plate capacitor in which the deflection of the cantilever can be monitored via a capacitance bridge [27][28]. This was also the case in the torquemeter developed by El Hallak [19] in Stuttgart, which served as basis for this work. While keeping the cantilever the same, two optical approaches to detect the deflection of the cantilever will be used - optical beam deflection and interferometry. Both detection schemes will be properly described in the second chapter, here the theoretical background for torque magnetometry will be briefly discussed.

A magnetised sample in a uniform magnetic field experiences a torque

$$\boldsymbol{\tau} = \mathbf{M} \times \mathbf{B}, \tag{1.3}$$

where $\mathbf{M} = (M_x, M_y, M_z)$ is the magnetization of the sample and $\mathbf{B} = (B_x, B_y, B_z)$ the external magnetic field [29]. Let us consider a coordinate system as defined in Fig. 1.5.

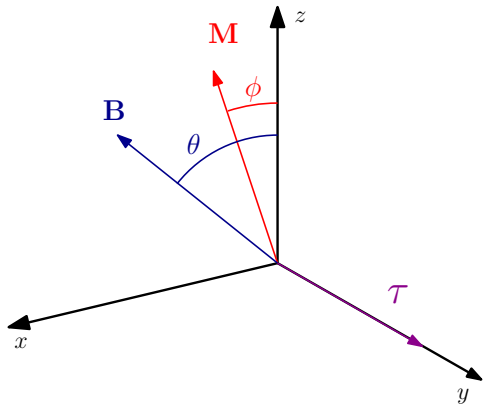

Fig. 1.5: General arrangement of a magnetised sample with magnetization **M** in an external magnetic field **B** resulting in induced torque $\boldsymbol{\tau}$.

Without loss of generality we can position both B and M into the xz plane. The cross product from eq. (1.3) then gives

$$\tau_y = B^2 \left(\frac{M_z}{B_z} - \frac{M_x}{B_x} \right) \sin\theta \cos\theta. \tag{1.4}$$

As we can see from eq. (1.3), the reason for induced torque is the non-collinearity between the applied magnetic field and sample magnetization. The origin of this phenomenon is different for ferromagnets and paramagnets. In the former, a spontaneous magnetic moment exists, which is fixed with respect to the samples crystallographic axes and it's direction with respect to the magnetic field depends only on

the sample orientation. If we orient the spontaneous moment, for example, in the z direction ($\phi = 0$), eq. (1.4) simplifies to:

$$\tau_y = BM \sin\theta \tag{1.5}$$

Important to note here is that the torque τ is simply proportional to the bulk magnetization M and that it vanishes for $n\pi$ (where n is an integer).

On the other hand, in paramagnets the magnetic moment is field-induced and the transverse magnetization components (in our case M_x) are a direct consequence of the paramagnetic anisotropy [29]. For our purposes we will consider a system with an easy-axis type anisotropy, i.e. that the magnetization has a preferential orientation at low temperature (for example z direction). This system will behave differently in weak ($g\mu_B B \ll k_B T$) and strong ($g\mu_B B \gg k_B T$) field limits. In weak fields the magnetization is simply given by $\mathbf{M} = \chi\mathbf{B} = (\chi_{xx}B_x, \chi_{yy}B_y, \chi_{zz}B_z)$. Consequently, the torque is given by

$$\tau_y = B^2 \left(\chi_{zz} - \chi_{xx}\right) \sin\theta \cos\theta. \tag{1.6}$$

Notice that the torque is zero for $\theta = n\pi/2$ with extremes at $n\pi/4$. In high fields the quadratic dependence on B breaks down and the torque will saturate to a limiting value of

$$\lim_{B\to\infty} \tau = -2DS(S - 1/2) \cos\theta \sin\theta, \tag{1.7}$$

defined by the systems axial anisotropy parameter D and the magnetic ground state S.

Thus by properly orienting the cantilever and the sample with respect to the magnetic field B and measuring it's deflection, we can probe the magnetic torque acting upon the sample - an example can be seen on Fig. 1.6.

1.3.2 Torque detected electron spin resonance

The combined method of CTM and broadband ESR, developed at the University of Stuttgart was named TDESR [19]. This method measures a change of magnetization in an magnetically anisotropic sample induced by a magnetic resonance transition. The torque of an ensemble of N spins with spin S depends on the population of the individual spin states ($M_S = -S,\ -S{+}1, \ldots, 0, \ldots, S{-}1,\ S$). The population abides the well-known Boltzmann distribution and total torque can then be expressed as

$$\tau = \sum_{N,M_S} \frac{\tau_{M_S} \mathrm{e}^{-\beta E_{M_S}}}{Z(B,T)}, \tag{1.8}$$

where τ_{M_S} is the torque of an individual spin in the M_S state, $Z(B,T)$ is the partition function and $\mathrm{e}^{-\beta E_{M_S}}$ describes the weight of each τ_{M_S} at a temperature T, since

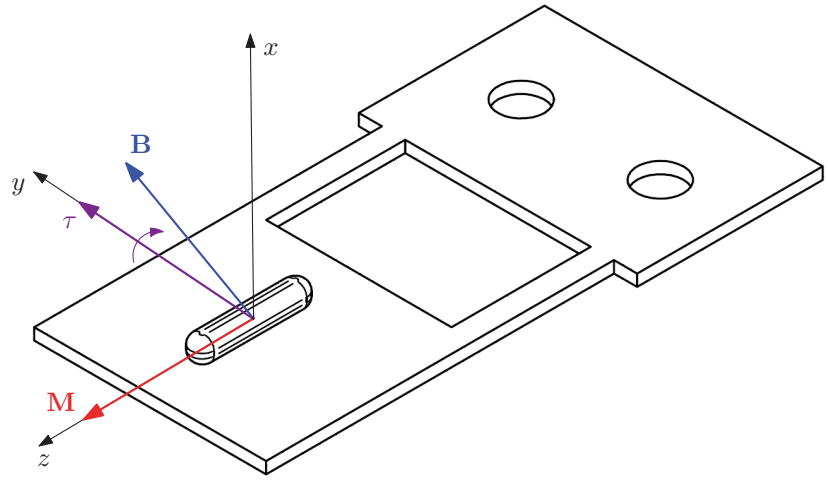

Fig. 1.6: An example of placement of the sample and the cantilever with respect to the magnetic field. In this configuration, the resulting torque will cause a movement of the cantilever in the x direction

$\beta = 1/(k_{\mathrm{B}}T)$, where k_{B} is the Boltzmann constant [30]. As we can see, the relationship is temperature dependent, therefore we will observe different torque signals at different temperatures. MW induced magnetic resonance transitions will also modulate the population difference, but only of two particular states between which the transition is induced. A MW photon with the energy of hf will induce a transition between two states satisfying the selection rule $\Delta M_S = \pm 1$, decreasing the population of the initial state while increasing the population of the final state. The total torque value is then changed depending on the instantaneous population of the two states. In the experiment we measure the torque without irradiation, which gives us τ_{u} and under irradiation (τ_{irr}). The difference between the two signals

$$\Delta\tau = \tau_{\mathrm{u}} - \tau_{\mathrm{irr}}, \tag{1.9}$$

then gives us an ESR-like spectrum (Fig. 1.7). If we are interested only in the ESR signal, we can treat the magnetization curve as a baseline effect and extract just the peaks of interest.

1.4 Comparison of ESR and TDESR spectrometers

In this section we will introduce the basic parts typical ESR spectrometers should contain. A simplified block representation will be used, since the possible variations, extensions and upgrades are almost innumerable. We will consider both ESR

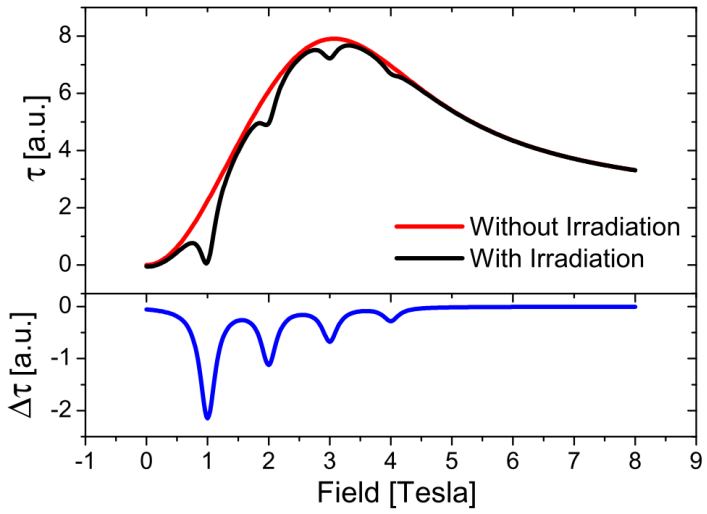

Fig. 1.7: A simulation depicting the torque signals of irradiated and non-irradiated sample (top). An ESR line-shape is the result of subtraction of the two signals. Figure taken from [30].

detected via MW absorption and via magnetization measurement. A detailed description of our setup can be found in section 4.1.2.

Generally, we can divide an ESR spectrometer into 4 parts - MW source, MW propagation system, cavity (or a sample holder) and MW detection (Fig. 1.8). In the case of TDESR MW detection is optional, but generally is also used to monitor the MW power or to correctly align the irradiation (Fig. 1.8b).

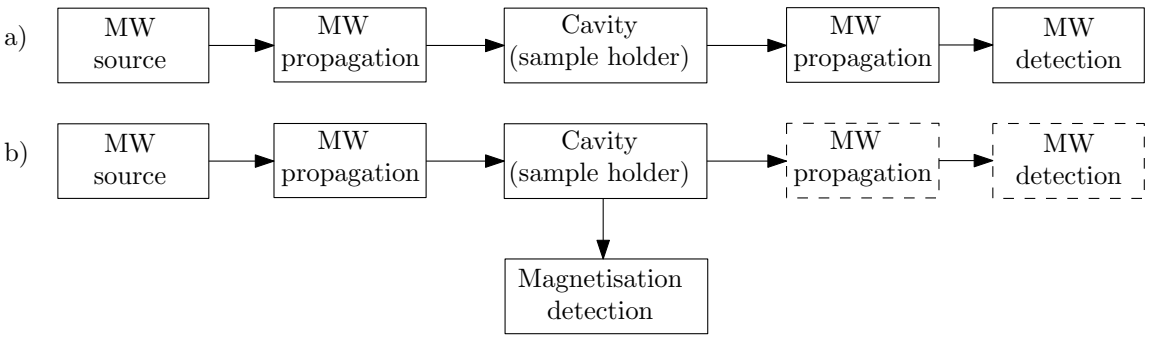

Fig. 1.8: Schematic representation of an ESR spectrometer, with: a) MW absorption detection (ESR); b) magnetization detection (TDESR).

Microwave source: In the past, the most used MW source was a vacuum tube called klystron, later other types of vacuum tube oscillators were developed and some are still used today (e.g., orotrons, gyrotrons or, in our case, Backward-Wave Oscillators (BWOs), see Fig. 1.9). Nowadays most widely used are solid state sources in combination with frequency multipliers, such as phase-locked Gunn diodes or dielectric resonance oscillators (DROs). There are other sources available, but their use is rather rare compared to those mentioned [5].

Microwave propagation: For effective propagation and focus of the MW radiation two options can be used, either waveguides or free space QO propagation.

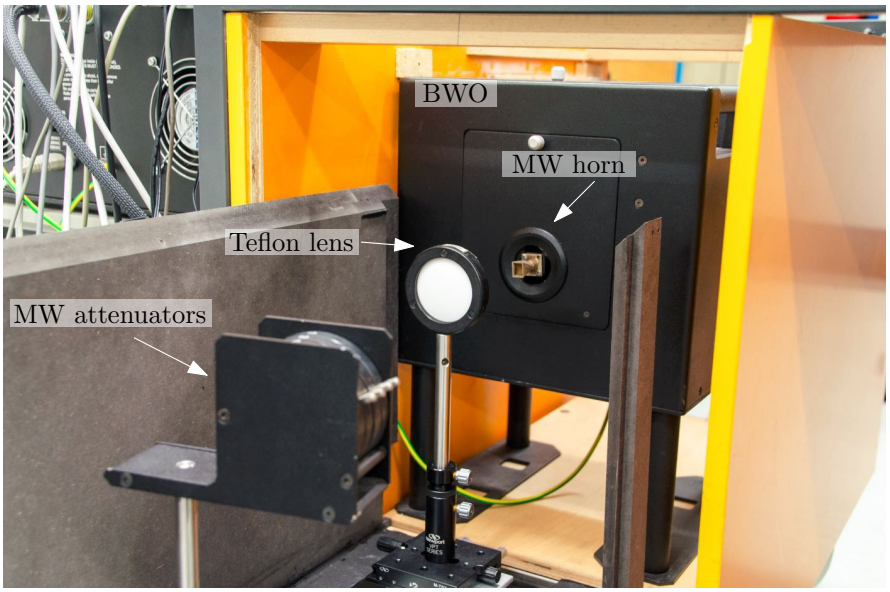

Fig. 1.9: Typical THz backward wave oscillator, along with other quasi-optical elements used in our setup - a metal horn to couple the MW to the free space, a teflon lens to focus or collimate the beam and a set of MW attenuators.

In the frequency range below 100 GHz, usually the former is used, which means that the radiation is propagated via waveguides (circular/rectangular metal tubes, either single-mode or oversized). However, at higher frequencies single-mode waveguides become very lossy, which can be overcome either by oversized corrugated waveguides (see Fig. 1.10a) or QO components (see Fig. 1.10b, Fig. 1.9).

Cavity or a sample holder: In conventional ESR, to maximize interaction of the MW radiation with the sample, resonant cavities are usually employed. The exact type of cavity (e.g., single mode cavity, Fabry-Pérot resonator, etc.) depends on the studied sample and used MW frequencies. However, at higher frequencies (above 200 GHz) manufacturing of single mode cavities becomes challenging, and at even higher frequencies very impractical (for example at 300 GHz the size of a single mode resonator is 0.5 mm). At those frequencies cavities are replaced by oversized sample holders, with shape and size depending on the experimental setup (single pass transmission, reflection, etc.). Since samples should be (but not necessarily must, e.g., for zero field FDMR) in an external magnetic field, these cavities or sample holders are usually placed inside a magnet (resistive or superconductive) combined with a cryostat to measure at low temperatures. In TDESR the sample is directly placed on the cantilever in an optical magnet and the MW radiation is directed and focused upon the cantilever with a teflon lens.

Detection system: For the observation of MW absorption lines in conventional ESR, numerous solid state detectors are used (such as bolometers or Schot-

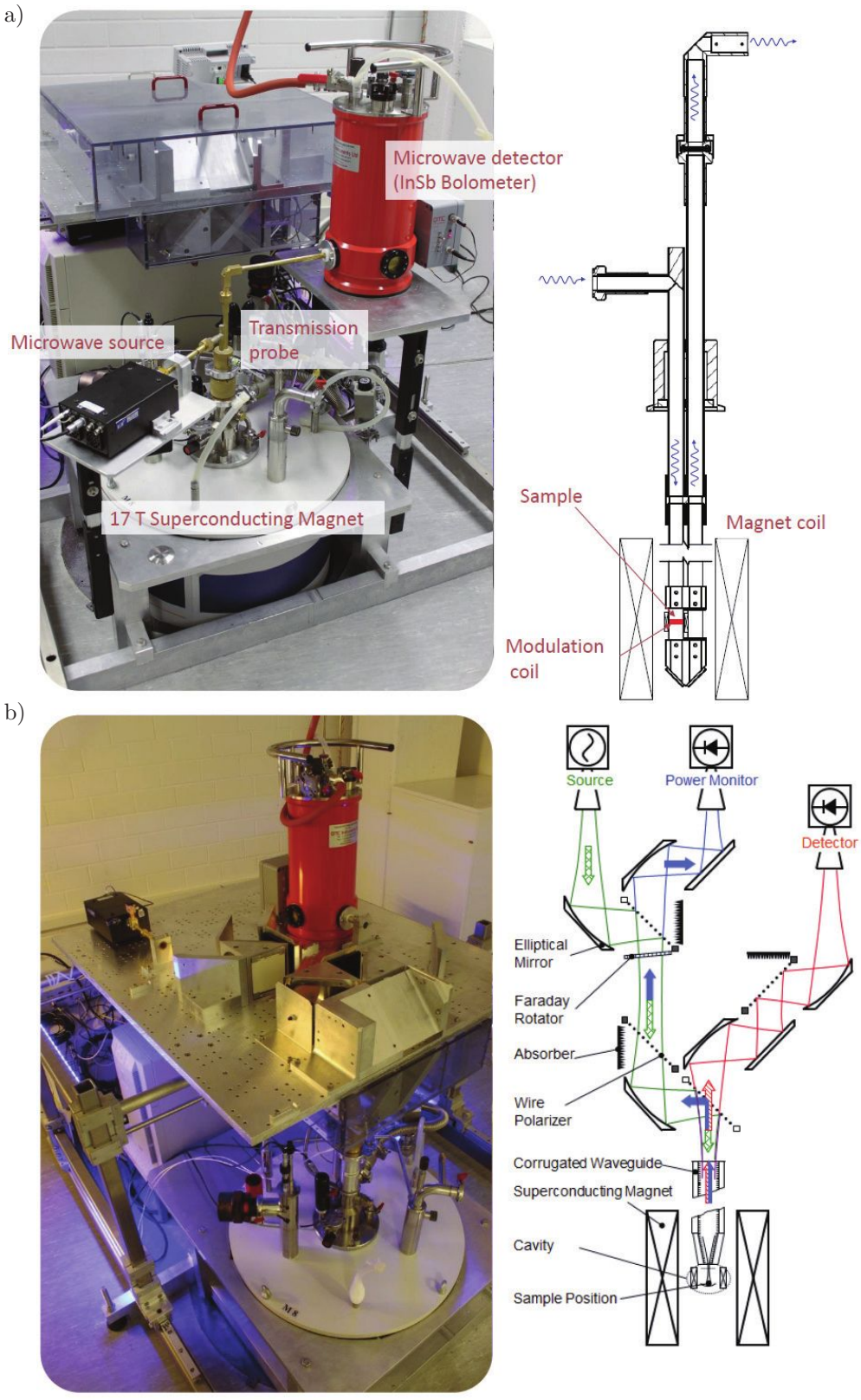

Fig. 1.10: High field EPR setups at the University of Stuttgart. a) Transmission setup using oversized waveguides (brass pipes), b) reflection setup using only QO components and a corrugated waveguide.

tky diodes). However, the direct detection of the absorption signal is possible only for samples containing high concentration of unpaired electrons - due to noise components, spanning a wide range frequencies, usually drown out the desired signal. Therefore almost always lock-in techniques are used, where a small modulated magnetic field is applied in addition to the main magnetic field at a preselected frequency. This frequency is then superimposed on the detected signal and amplified, which significantly improves the signal-to-noise ratio. The field modulation technique also results in detection of first derivative of the absorption spectrum (see Fig.1.11).

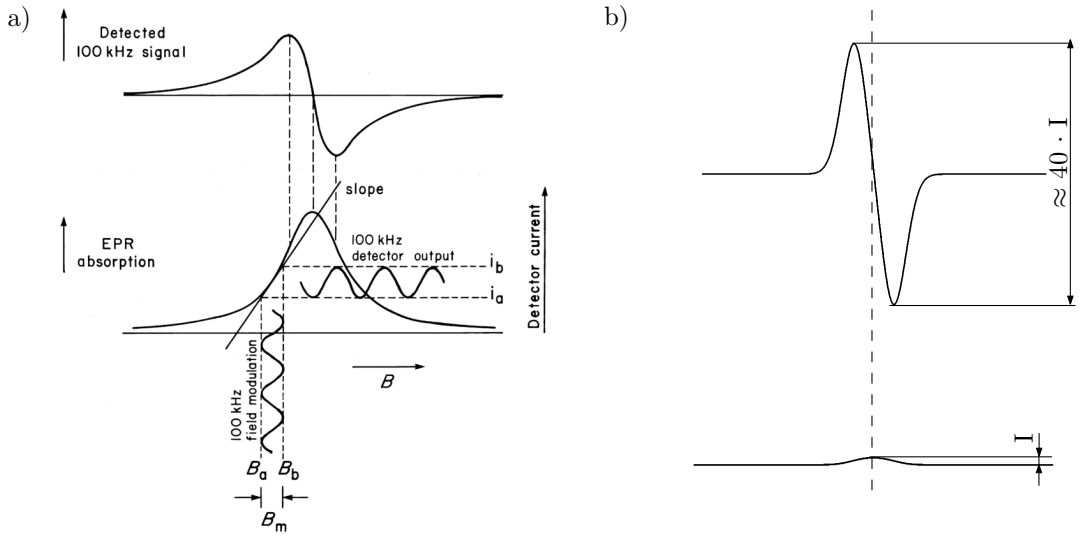

Fig. 1.11: a) Effect of small-amplitude 100 kHz field modulation on the detector output current. The static magnetic field B is modulated between the limits B_a and B_b. The corresponding detector current varies between the limits i_a and i_b. Not to scale, taken from [4]; b) Simulated effect of field modulation in terms of intensity improvement. Assuming that the difference between maximum and minimum value of the absorption intensity is I, the same value for a modulated signal can be, depending on the linewidth and modulation amplitude, almost forty times higher. Simulation was done using Easyspin toolbox for Matlab [31].

When detecting ESR via a change in magnetization, MW absorption lines are detected via a difference in the magnetization curve under MW irradiation (Fig. 1.7), therefore the detection system depends on the type of magnetometry that is performed. As we are using CTM, we need to detect subtle movements of our cantilever, which can be done in multiple ways. When using AFM microcantilevers, one can detect the magnetization change via a change in resistance of a piezoresistive element. Another option is to form a parallel-plate capacitor with the cantilever acting as one plate. The capacitance can then be measured via a capacitance bridge to obtain the magnetization curve. This method was used for TDESR before [19] and served as basis for this work. Optical methods used in AFMs, i.e. optical beam deflection

and interferometry, which we have implemented in this work. will be discussed in chapter 2.

1.5 Single molecule magnets

A molecular magnet is a molecule comprising of one or more magnetic centers (which can be transition metal ions, lanthanides or both) coupled via exchange interaction resulting in a net total spin of the molecules. These atoms are surrounded by an array of bound molecules, known as ligands, which can greatly modify their chemical properties and can be tuned with great precision. Molecular magnets with an easy-axis type anisotropy (also called Ising-type anisotropy) were coined with the term SMMs. Direct consequence of the preferential orientation of their spin is the slow relaxation of magnetization below a certain blocking temperature T_{B}. Below this temperature, the orientation of their total spin can be preserved for very long time (e.g., $\approx 40\,$years at $1.5\,$K for $Mn_{12}Ac$), which makes it in principle possible to store information in a single molecule [32]. Their magnetization curves display not only hysteresis, but sometimes also a step-like shape of the hysteresis curves (Fig.1.14), which is a signature of Quantum Tunnelling of Magnetisation (QTM) [33]. The quantum behaviour of magnetisation can be in principle exploited for development of quantum computing [32].

The first complex identified to behave as a SMM was the dodecanuclear manganese cluster

$$[Mn_{12}O_{12}(CH_3COO)_{16}(H_2O)_4] \cdot 2CH_3COOH \cdot 4H_2O,$$

with a groun spin state of $S = 10$ [34] (Fig.1.12a). Since then, many others were successfully synthesized, although $Mn_{12}Ac$ long held the record of the highest energy barrier for reversal of magnetization. Another typical representative, studied in this work, is the Fe_4 SMM with a propeller-like structure and a $S = 5$ spin ground state (Fig.1.12b).

The ground spin state of SMMs is usually described by the Giant Spin Hamiltonian. Up to the second order for the so called Zero-Field Splitting (ZFS), this Hamiltonian has the form

$$\mathcal{H} = \mathcal{H}_{\mathrm{Z}} + \mathcal{H}_{\mathrm{LF}} = \mu_{\mathrm{B}} \hat{\mathbf{S}} \cdot \mathbf{g} \cdot \mathbf{B} + D[\hat{\mathbf{S}}_{\mathrm{z}}^2 - \frac{1}{3}S^2] + E(\hat{\mathbf{S}}_{\mathrm{x}}^2 - \hat{\mathbf{S}}_{\mathrm{y}}^2), \qquad (1.10)$$

where $\mathcal{H}_{\mathrm{Z}} = \mu_{\mathrm{B}} \hat{\mathbf{S}} \cdot \mathbf{g} \cdot \mathbf{B}$ is the Zeeman Hamiltonian, $\mathcal{H}_{\mathrm{LF}}$ is the ligand field Hamiltonian which contains the axial and rhombic ZFS parameters D and E respectively and $\hat{\mathbf{S}}_{\mathrm{x}}, \hat{\mathbf{S}}_{\mathrm{y}}^2, \hat{\mathbf{S}}_{\mathrm{z}}$ are components of the spin operator $\hat{\mathbf{S}}$. Values of the second order ZFS parameters D and E are restricted by the relationship: $-1/3 \leq E/D \leq 1/3$. When

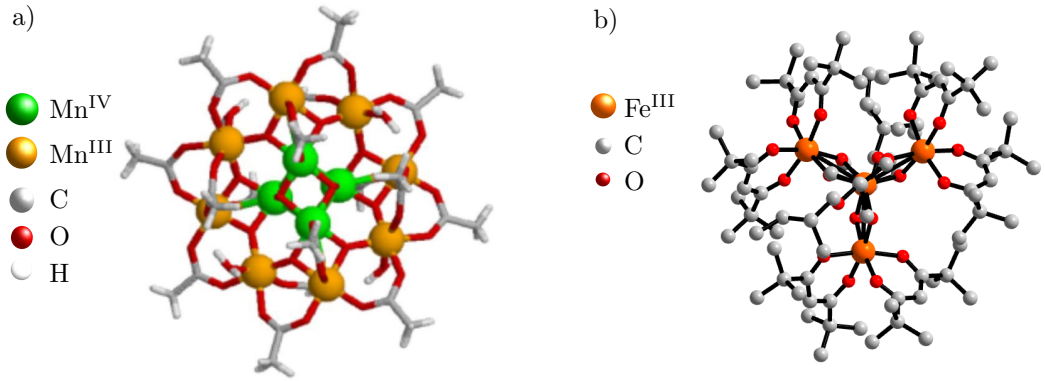

Fig. 1.12: Famous single molecule magnets: a) The first SMM complex, $Mn_{12}Ac$; b) SMM studied in this work, tetrairon(III) complex. Structures taken from [35].

the ratio $|E/D| = 1/3$, the system is fully rhombic, whereas when $E = 0$ the system is fully axially symmetric. D can be either negative or positive, corresponding to an easy-axis or easy-plane type anisotropy. This ligand field Hamiltonian is the simplest approximation for magnetic anisotropy of the system. Dealing with large spin values S it is necessary to include higher order terms - the complete Hamiltonian is then

$$\mathcal{H} = \mathcal{H}_{\mathrm{Z}} + \mathcal{H}_{\mathrm{LF}} = \mu_{\mathrm{B}} \hat{\mathbf{S}} \cdot \mathbf{g} \cdot \mathbf{B} + D[\hat{\mathbf{S}}_{\mathrm{z}}^2 - \frac{1}{3}S^2] + E(\hat{\mathbf{S}}_{\mathrm{x}}^2 - \hat{\mathbf{S}}_{\mathrm{y}}^2) + \sum_{k,q} B_k^q O_k^q, \qquad (1.11)$$

where O_k^q are Stevens operators and B_k^q are corresponding parameters [5][4]. This Hamiltonian can be used to calculate ESR spectra using the Easyspin package for Matlab [31]. For the Fe_4 SMMs the fourth order terms will be considered in addition to the second order terms.

As SMMs have an easy-axis type anisotropy, their spin ground state S is split by a negative D. In the ground multiplet are then the levels with highest M_S quantum number lowest in energy (and vice versa), while the energy barrier for reversal of magnetization is $\approx DS^2$ (Fig.1.13a). Application of a positive external magnetic field leads to a preferred population of the $M_S = -S$ state, corresponding to a preferred orientation along the external magnetic field (Fig.1.13b). Relaxation of the magnetization can take place thermally via phonons, but at low temperatures only QTM is possible. QTM can take place only between energy levels, which coincide on both sides of the barrier. This behaviour can be seen in Fig. 1.14.

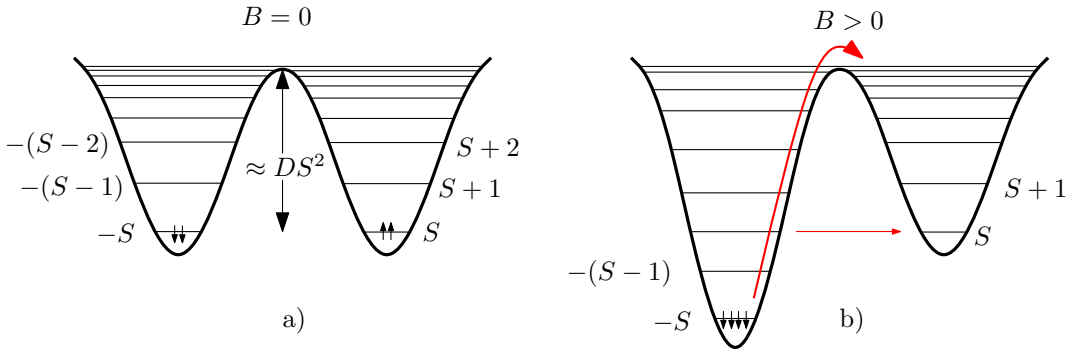

Fig. 1.13: A schematic representation of the magnetization states as a double-well potential with M_S energy levels for a SMM with total spin S and easy-axis type anisotropy at finite temperature: a) System at zero magnetic field; b) In a non-zero magnetic field, the sample is polarised to the -S state. The SMM can relax from the -S state (overcome the potential barrier $\sim DS^2$) either by QTM, multiple Orbach processes or a combination of both. QTM can take place only when the energy levels on both sides of the barrier coincide.

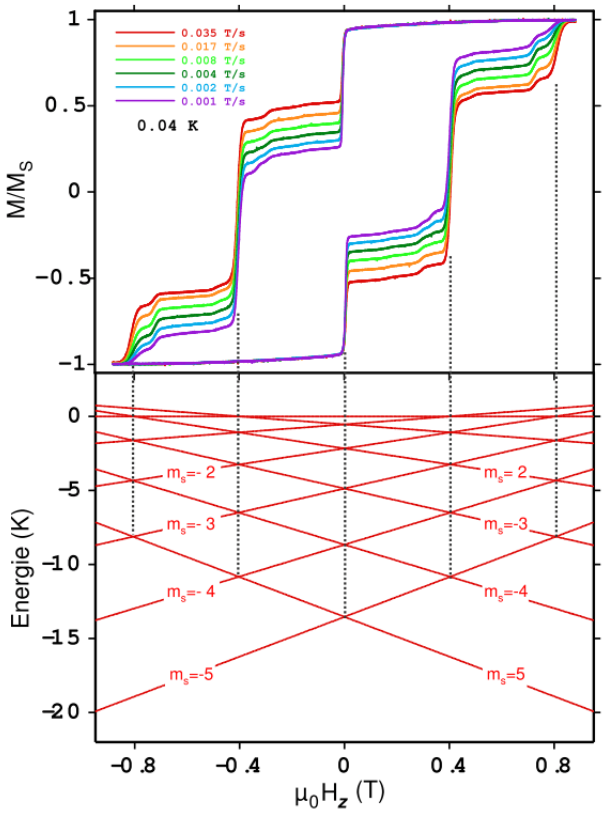

Fig. 1.14: magnetization hysteresis curve of SMM Fe4 with $S = 5$ measured by micro-SQUIDs. The step-like shape of the curve is a typical feature of SMMs. The steps correspond to increase in the rate of magnetization change via QTM when energy levels on both sides of the potential barrier coincide (Fig.1.13), as seen on the Zeeman diagram below. Picture taken from [5].

2 OPTICAL DETECTION OF CANTILEVER DEFLECTION

The measurement of subtle deflections of cantilevers is a well-researched area, mainly thanks to atomic force microscopy. In the original AFM setup by Binnig, Quate and Gerber in 1986 a tunneling junction was used to monitor the displacement of the cantilever [36] - shortly after, in 1987 a slightly less complicated detection method was implemented by McClelland, Erlandsson and Chiang, based optical interferometry [37]. Another year later, an even simpler method was successfully implemented by Meyer and Amer, the so called laser beam deflection [38]. This method then became most widely used in AFMs due to it's high sensitivity and simplicity. In our setup we have used both laser beam deflection and optical interferometry to inspect which method is more suitable for our purposes. After introduction of these methods we will estimate the deflections of the cantilever and the sensitivity for both setups. In the last section we will describe the experimental setup and design of the measurement probe.

2.1 Laser beam deflection setup

In this method a weak (few mW) laser is directed on the backside of a cantilever, from where it is reflected onto a Position Sensitive Detector (PSD). We have used a diode laser with integrated lens (Thorlabs CPS198, Fig. 2.1a), which gave us the possibility to easily adjust the focus and quickly find the optimum for our experiments. A compact laser diode was chosen due to its availability and small size, which gave us the option to use it both for bench-top proof-of-concept measurements and our space-limited setup utilizing low temperatures and high magnetic fields. Our laser emits an elliptical spot of the wavelength 670 nm at 4.5 mW power, which can be focused (50 mm - ∞) via turning of the integrated lens. For the detector we have chosen a commercial 2D PSD module (Hamamatsu C1443-01, Fig. 2.1b), which detects the laser spot via photocurrent from 4 electrodes, positioned on the sides of the active area. The signal is further processed and amplified in a commercial signal processing module (Hamamatsu C10460, Fig. 2.1c) and sent to the PC via RS232 standard. This PSD has a $4 \times 4\,\mathrm{mm}^2$ active area with 16-bit digital output in both vertical and horizontal directions, which translates into a theoretical positional resolution of $\approx 0.06\,\mu\mathrm{m}$ - the manufacturer states an effective resolution of $0.5\,\mu\mathrm{m}$. A schematic diagram of this setup can be seen in Fig. 2.2.

This method has provided us with excellent measurements with respect to capacitive detection, which can be seen in chapter 4. The biggest disadvantages are

however the need for optical access from both sides (for MW radiation from one side, for laser for the other, in case of TDESR) and limited rotational capability, since after each change of angle of the cantilever with respect to the magnetic field, the PSD has to be repositioned (in case of CTM).

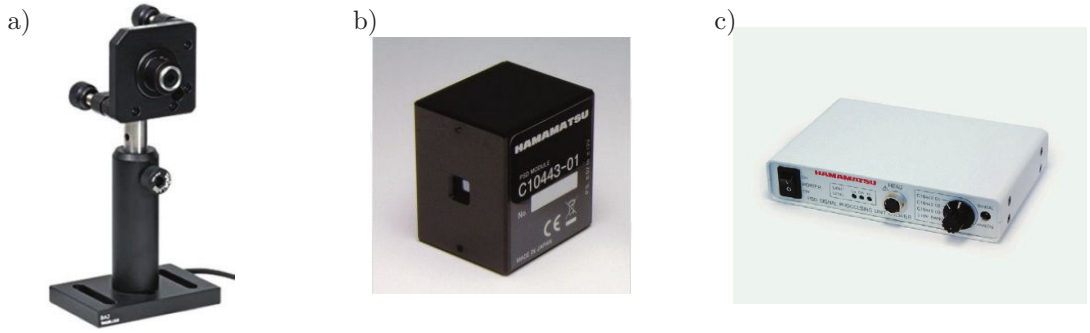

Fig. 2.1: Equipment for laser beam deflection. a) CPS198 Laser diode from Thorlabs mounted in a kinematic mount [39], b) C1443-01 PSD module from Hamamatsu [40], c) C10460 signal processing unit for PSD from Hamamatsu [41].

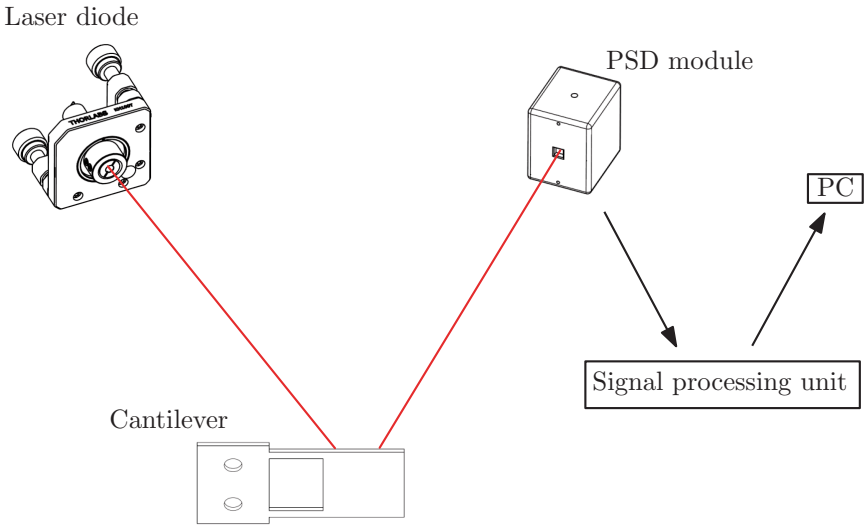

Fig. 2.2: A schematic diagram of the laser beam deflection setup.

2.2 Interferometric detection setup

The fiber-optic interferometer was designed and built by Dalibor Šulc from Brno University of Technology, based on the work of Rugar [42]. A schematic diagram of the setup can be seen in Fig. 2.3. A HeNe laser (635 nm output, from Lasos) is coupled with an objective to a single mode FC/PC optical fiber (Thorlabs 630HP), which is connected to an optocoupler (a 90:10 coupler was not available during initial

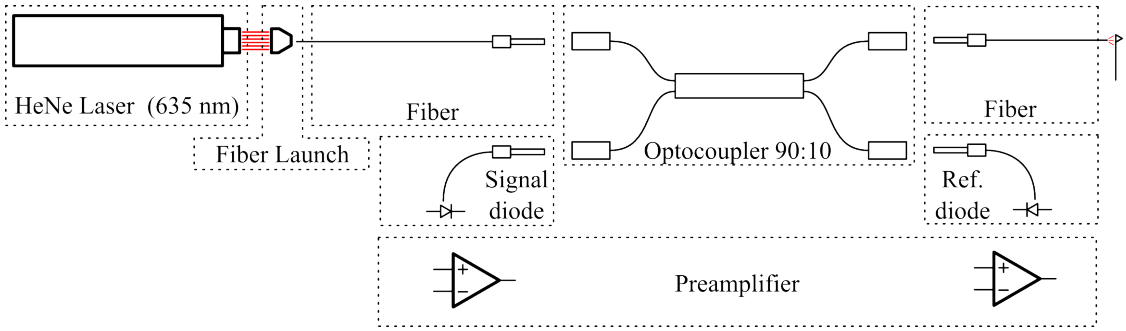

Fig. 2.3: Schematic diagram of used fiber interferometer. Image courtesy of Dalibor Šulc.

testing, therefore an 50:50 FC/PC Thorlabs FC632-50B-FC was used). This coupler splits the incident light in the given ratio between the fiber used for measurement and a reference diode on the preamplifier, designed and built by Dalibor Šulc. In the signal fiber, part of the incident light is reflected from the fiber core - air interface, rest of the light is transmitted, exits the fiber, impinges on the cantilever and is scattered back into the fiber, where it interferes with the light reflected from the fiber-air interface. On the preamplifier signal diode we can then observe an interference pattern. To estimate the reflected portion, we can use the Fresnel equation for reflection at normal incidence

$$R = \left(\frac{n_c - n_a}{n_c + n_a}\right)^2, \tag{2.1}$$

where n_c is the index of refraction of fiber core (1.145530, from the manufacturers catalogue [43]) and n_a index of refraction of air (1). We can then readily see that $\approx 3.4\%$ is reflected at the interface. We can then model the process as a simple two-component interference, since multiple reflections can be neglected (Fig. 2.4).

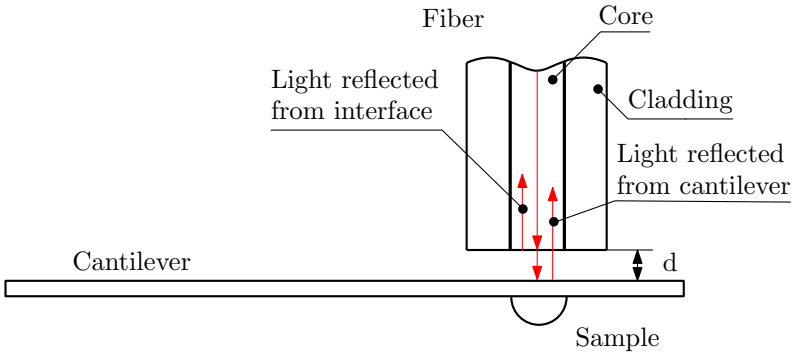

Fig. 2.4: Detail of the interferometer cavity for TDESR.

The total optical power directed back through the fiber and onto the signal diode depends on the phase difference between the light reflected from fiber end and the cantilever reflection

$$I = I_1 + I_2 + 2\sqrt{I_1 I_2}\cos\left(4\pi\frac{d}{\lambda}\right), \tag{2.2}$$

where I_1 and I_2 are the intensities of the interfering waves, d is the fiber-cantilever distance and λ is wavelength of used light. In Fig. 2.5 we can see a simulated signal for the 635 nm laser. Depending on the magnitude of deflections we wish to detect, two modes of signal readout and interpretation can be implemented. If we expect deflections only at the order of nanometers, we can set the distance between the fiber tip and the cantilever to it's most sensitive point (integer multiples of $\lambda/8$, $\approx$ 79.4 nm in this case) and look only at the linear signal in the $\approx$ 80 nm region around this point. Beyond this region, the signal is no longer linear and beyond $\lambda/4$ (158,75 nm) the signal becomes ambiguous and we will have to resort to a technique of counting the interference fringes, which can be more complicated for data acquisition software. Due to large differences in signal strengths of various samples, both cases have to be accounted for.

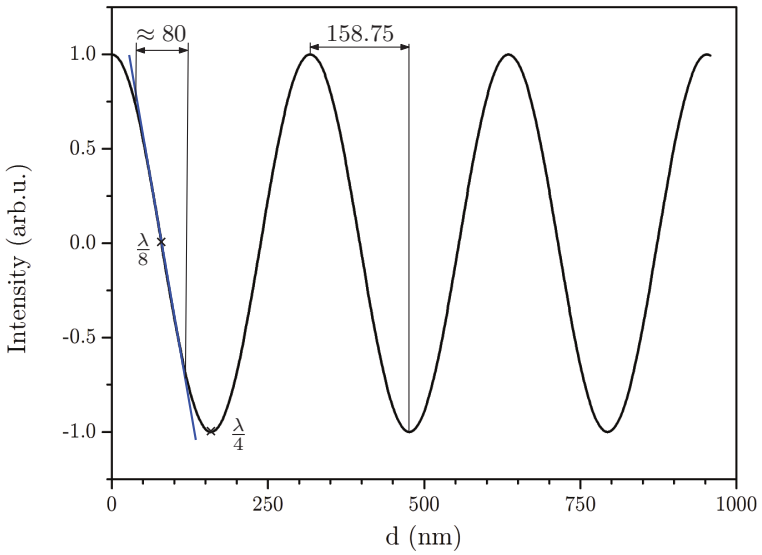

Fig. 2.5: Simulated interference signal on the detector as a function of distance between the fiber tip and cantilever. Emphasized are the $\approx$ 80 nm approximately linear section, where the system is most sensitive, and the 158.75 nm range where the signal is unambigious. Simulated for 635 nm laser.

2.3 Calculation of cantilever deflection

We have established in section 1.3.1 that by probing the deflection of a cantilever, we can measure the magnetization of a sample and therefore observe ESR. To get an estimate of the sensitivity and expected deflections of the cantilever, we can calculate the deflection analytically and numerically via Finite Element Analysis (FEA).

2.3.1 Analytical approach

This calculation is based on the theory of elasticity, found for example in the book on Mechanics of Materials by Hibbeler [44]. Consider a cantilever as defined on Fig. 2.6. We will simplify the calculation by two assumptions. First, we replace

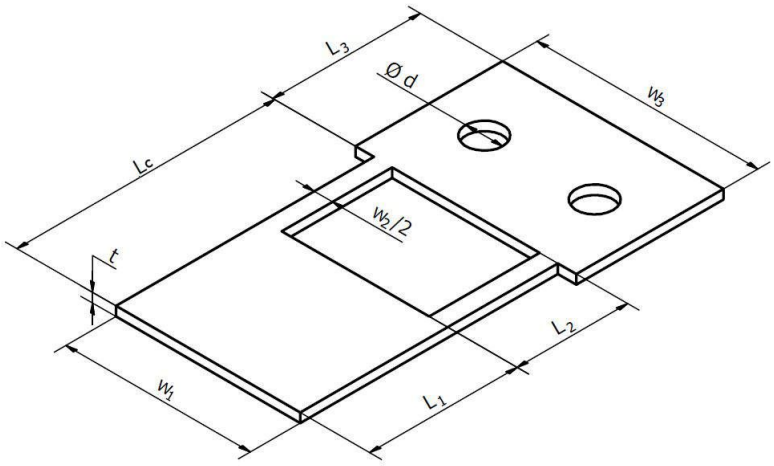

Fig. 2.6: Drawing of used macrocantilever with dimensions used in the calculation.

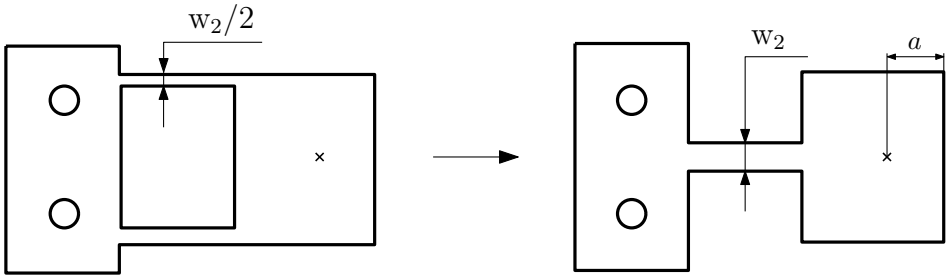

Fig. 2.7: Replacement of a double-arm with a single-arm cantilever. The sample position is indicated by an x, with distance from the end of the cantilever a.

the two thin beams of width $w_2/2$ by one central beam of width w_2 (Fig. 2.7). The second assumption is that behind the position of the sample, i.e. the point where the torque is applied, the cantilever is no longer bent and the final deflection can be calculated by linear extension. If we calculate the deflection only for small angles, the linear extension can be calculated just by $a \cdot \tan\theta \approx a \cdot \theta$ (Fig. 2.8), where θ is the angle of the deflected beam and a the distance of the sample (point of the applied torque τ) from the end of the cantilever. Therefore, we can model our situation as a cantilevered beam with a torque acting upon its free end.

To calculate the deflection ν of any beam, we must solve the differential equation

$$\frac{\mathrm{d}\nu^2}{\mathrm{d}x^2} = \frac{M(x)}{EI}, \tag{2.3}$$

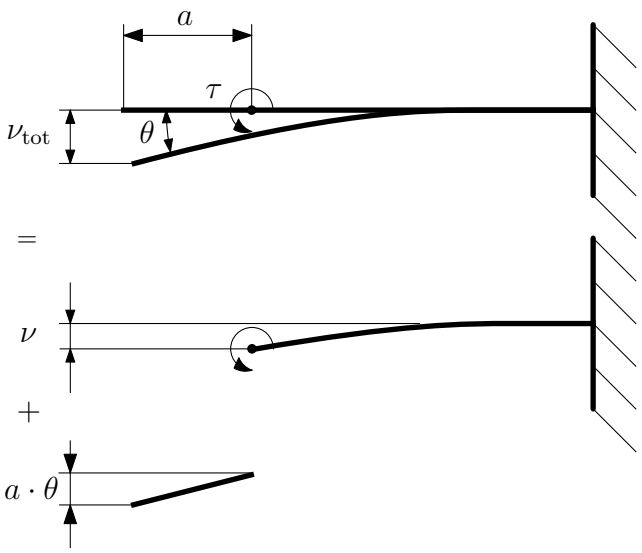

Fig. 2.8: The total deflection ν_{tot} is calculated as a sum of deflection at the point of applied torque τ (sample position) and a linear extension of the cantilever.

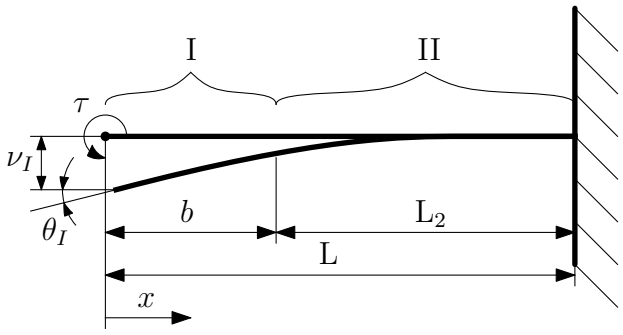

Fig. 2.9: Schematic drawing of model beam and quantities used in the calculation of deflection of section I (ν_{I}) from torque τ, b is the length of section I (L_1 - a) and x shows the direction of the x axis.

where M is the total internal moment of the beam, i.e. the sum of all moments acting upon the beam, E is Young's modulus of the material and I the moments of inertia of a given cantilever. In order to solve this equation by integration, we must first divide the cantilever into sections where the expression M/EI is constant. Our cantilever has two sections with different moments of inertia I, section I (with the width w_1 and length b) and II (with width w_2 and length L_2). Their moments of inertia are

$$I_{\mathrm{I}} = \frac{w_1 t^3}{12} \qquad I_{\mathrm{II}} = \frac{w_2 t^3}{12}. \tag{2.4}$$

In our case, the total internal moment of the cantilever is just $M = -\tau$. We can integrate the equations for ν_{I} (deflection of part I) and ν_{II} (deflection of part II) separately

$$\frac{\mathrm{d}\nu_{\mathrm{I}}{}^2}{\mathrm{d}x^2} = -\frac{\tau}{EI_{\mathrm{I}}} \qquad \frac{\mathrm{d}\nu_{\mathrm{II}}{}^2}{\mathrm{d}x^2} = -\frac{\tau}{EI_{\mathrm{II}}} \tag{2.5}$$

$$\frac{\mathrm{d}\nu_{\mathrm{I}}}{\mathrm{d}x} = -\frac{\tau x}{EI_{\mathrm{I}}} + C_1 \qquad \frac{\mathrm{d}\nu_{\mathrm{II}}}{\mathrm{d}x} = -\frac{\tau x}{EI_{\mathrm{II}}} + C_3 \tag{2.6}$$

$$\nu_{\mathrm{I}} = -\frac{\tau x^2}{2EI_{\mathrm{I}}} + C_1 x + C_2 \qquad \nu_{\mathrm{II}} = -\frac{\tau x^2}{2EI_{\mathrm{II}}} + C_3 x + C_4. \tag{2.7}$$

To calculate the integration constants and bind the equations together, we will use boundary and continuity conditions. Since one end of the cantilever is fixed, there can be no displacement and there must be zero slope at that point. Since the central axis of the cantilever has to be a smooth, continuous curve, displacement and slope have to be equal from both sides of the border between parts I and II. Therefore we can write

$$\left.\frac{\mathrm{d}\nu_{\mathrm{II}}}{\mathrm{d}x}\right|_{x=L} = 0; \qquad \left.\frac{\mathrm{d}\nu_{\mathrm{II}}}{\mathrm{d}x}\right|_{x=b} = \left.\frac{\mathrm{d}\nu_{\mathrm{I}}}{\mathrm{d}x}\right|_{x=b} \tag{2.8}$$

$$\left.\nu_{\mathrm{II}}\right|_{x=L} = 0; \qquad \left.\nu_{\mathrm{II}}\right|_{x=b} = \left.\nu_{\mathrm{I}}\right|_{x=b}. \tag{2.9}$$

From these equations we can readily calculate the integration constants

$$C_1 = \frac{\tau b}{EI_{\mathrm{I}}} + \frac{\tau}{EI_{\mathrm{II}}}(L-b) \qquad C_3 = \frac{\tau L}{EI_{\mathrm{II}}} \tag{2.10}$$

$$C_2 = -\frac{\tau b^2}{2EI_{\mathrm{I}}} - \frac{\tau b}{EI_{\mathrm{II}}}(L-b) \qquad C_4 = -\frac{\tau L^2}{2EI_{\mathrm{II}}}. \tag{2.11}$$

We have now an analytical expression with which we can calculate the deflection and slope of the cantilever at any point. For control purposes, let us now consider one of the experimentally used cantilevers with dimensions stated in Tab. 2.1. Our cantilevers are chemically etched out of a $Cu_{98}Be_2$ alloy with Young's modulus of 120 GPa [45]. This material has excellent elastic properties even at cryogenic temperatures and can be purchased in a variety of thicknesses. To have a number for

Tab. 2.1: Parameters of the cantilever in mm.

w_1	w_2	w_3	L_1	L_2	L_3	t	d
4.5	1	6	4.5	3	4	0.08	1

comparison of the calculations, we applied a torque of magnitude 1×10^{-9} Nm, and with our analytical calculation, we have obtained a maximum deflection (i.e. the deflection at the end of the cantilever) of 2.9405 nm.

2.3.2 Finite element analysis

The FEA was done using the software Autodesk Inventor. The dimensions of the cantilever were the same as in Tab. 2.1. The simulation conditions and results can be seen in Fig. 2.10 and Fig. 2.11 respectively. We have applied a torque of magnitude 1×10^{-9} Nm and simulated deflection of 4.679 nm at the end of the cantilever - this discrepancy with analytical value may be due problems of FEA with thin materials and a proper calibrated measurement should be performed for certainty. In Fig. 2.11a we can also see that our second assumption was correct and no bending occurs after the point of applied torque, since there is no stress.

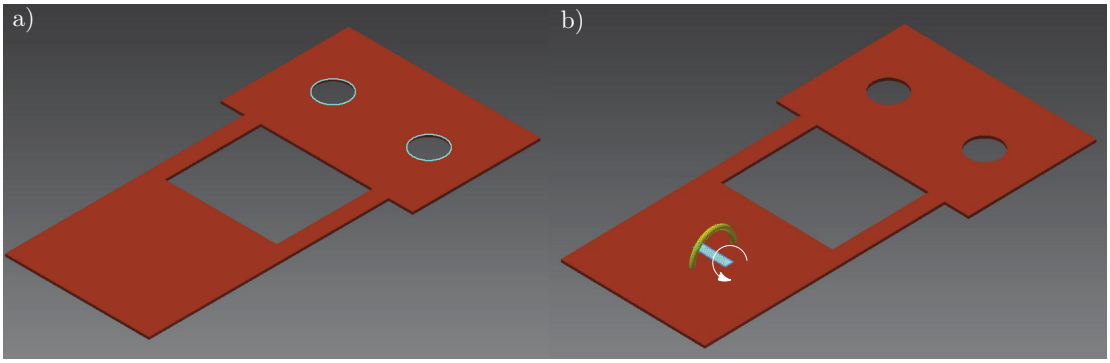

Fig. 2.10: Conditions of the FEA. a) Fixed constraint used on the holes, b) position of applied load.

2.3.3 Theoretical sensitivity of optical detection methods

Let us now consider the sensitivity of the optical beam deflection setup. Its sensitivity will mainly depend, apart from the mechanical properties of the cantilever, on the resolution of our PSD and the cantilever-PSD distance. Due to the nature of the used laser source and optical accessibility, the laser spot cannot be focused to a different point then approximately the middle of the cantilever, therefore we will calculate deflections at that point.

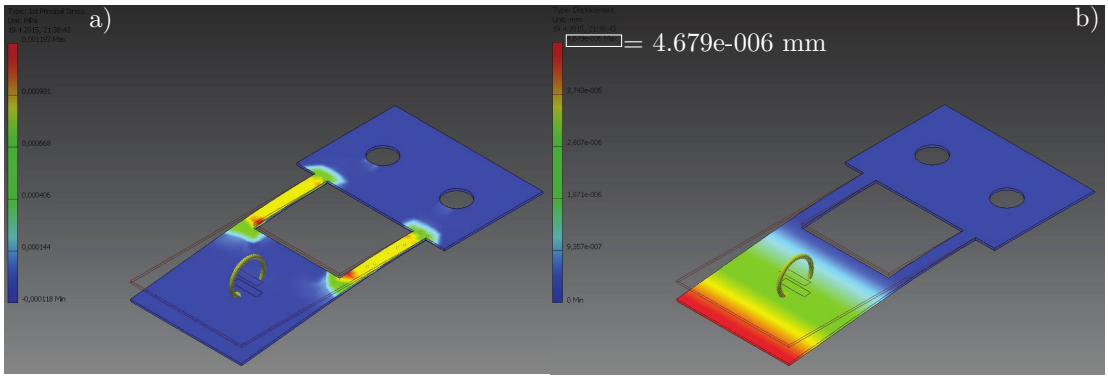

Fig. 2.11: Results of the FEA. a) Stress distribution in the cantilever; b) displacement of the cantilever, maximum value rewritten for visibility.

The resolution of our PSD is 0.5 µm and the largest possible cantilever-PSD distance is $d \approx 770\,\text{mm}$ due to the optical rail and height of the optical posts (but this could be eventually modified). Since we have obtained an analytical solution to the cantilever deflection, we can evaluate not only the deflection, but also the slope at given point. What we detect as a position change Δp at the PSD is actually the change of slope $\theta = \mathrm{d}\nu/\mathrm{d}x$. Therefore, for small angles (which is in our experiments always the case), we can use just a simple triangular approximation (as in Fig. 2.12) and say that

$$\tan\theta \approx \theta = \frac{\Delta p}{d}. \tag{2.12}$$

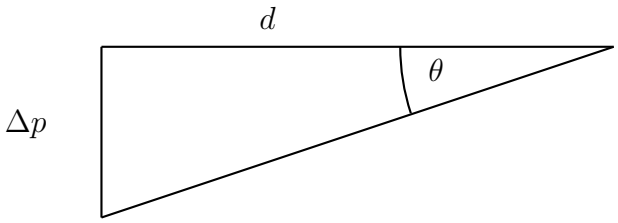

Fig. 2.12: Triangular approximation valid for small deflections used in sensitivity calculation.

To obtain a positional change of 0.5 µm at 770 mm the cantilever has to deflect at least 2.84 nm, which corresponds to an applied torque of $9.65 \times 10^{-10}\,\text{Nm}$. The active area of our PSD is 4 mm, which means the maximum deflection we can measure (at maximum distance) is 22.52 µm, caused by a torque of $7.66 \times 10^{-6}\,\text{Nm}$.

Sensitivity of the interferometric detection is determined by the number of different light levels that the photodiode can detect between light and dark, i.e. between an interference maximum and minimum and the wavelength of used laser. Since the photodiodes are analog devices, their resolution depends on the number of bits of

used analog-digital converter. Standard measurements cards have a 16 bit converter (32 and 64 bit converters are also available). The voltage from our photodiode can range from 0 to 10 V, this would however mean zero background light level, which is rarely achievable in an fiber-optic system due to reflections at interfaces and connectors. From experience, a reasonable range is from 2-10 V, i.e. 8 V in total. The difference between a minimum and a maximum is $\lambda/4$ of the used laser source, in the case of a HeNe laser 635 nm/4 = 158.75 nm, which gives us a sensitivity of 3 pm per bit. This sensitivity will be, however, overwhelmed by vibrational and electrical noise - even state-of-the-art commercial systems with 64 bit converters boast at best a 25 pm resolution. Therefore, a more realistic expectation based on experience would be on the order of tens of nanometers/nanometers, similar to the laser beam deflection, but with potential to go even lower with optimizations of the system.

3 DESIGN OF THE TDESR SPECTROMETER

This chapter is dedicated to the description of used experimental equipment. After describing the overal apparatus, the design of the TDESR probe will be introduced along with sample holders dedicated for different detection mechanisms. In the last section, LabView programs for system control and data acquistion will be described.

3.1 Overall setup

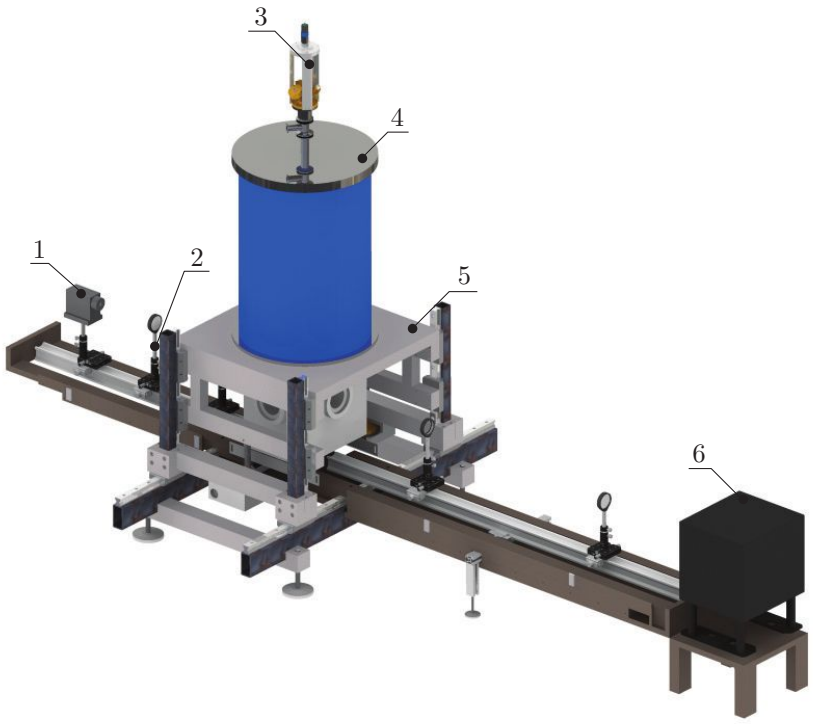

Fig. 3.1: An overall view of the experimental configuration for alignement of the MW. 1 - Golay cell, 2 - lens, 3 - TDESR probe, 4 - Spectromag, 5 - alignment table, 6 - BWO.

The TDESR spectrometer, depicted on Fig. 3.1, consists of two main parts: an optical magnet with a cryostat and a MW system consisting of an MW source, lenses and a detector. The magnet is the Spectromag SM4000 from Oxford Instruments, a magneto-optical system which can produce magnetic fields up to 10 T, featuring a Variable Temperature Insert (VTI) providing temperatures down to 1.5 K with optical access to the sample. The MW system is a set sold by Microtech Instruments. As MW source serves the BWO capable of producing basic frequencies from 155 GHz to 255 GHz. From there, the MW is collimated and focused with a system of MW lenses to the middle of the magnet, where the sample is located. During the MW alignment procedure, the sample holder can be put into such position that the MW

can travel freely to the other of the magnet, where a second set of lenses and a Golay cell are located (Fig. 3.2a). During a measurement with the laser deflection setup, the part behind the magnet is replaced with the laser diode and the PSD (Fig. 3.2b). For the interferometric detection, the MW detection part can be removed entirely (Fig. 3.2c), since the detection is carried out *in-situ* via an optical fiber.

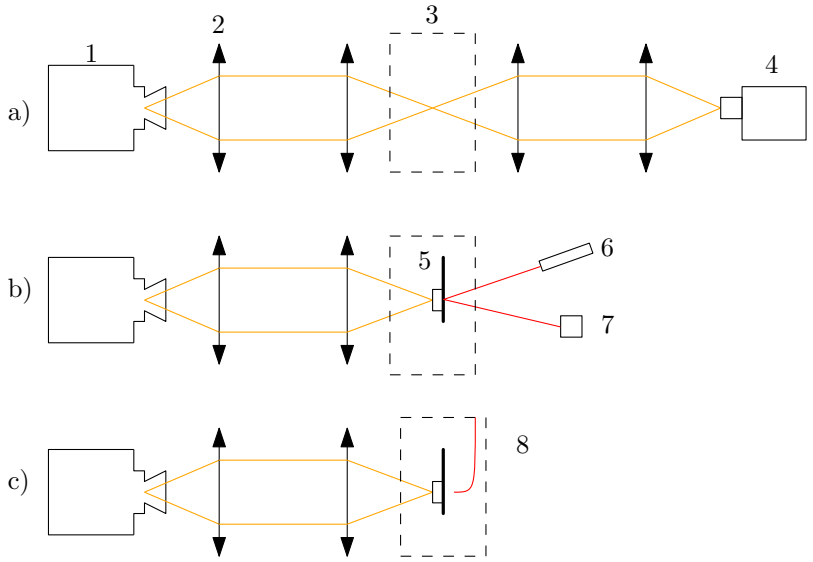

Fig. 3.2: Schematic overview of used experimental configurations. a) MW alignment configuration. 1 - BWO, 2 - lens, 3 - Spectromag, 4 - Golay cell; b) Laser beam deflection setup. 5 - cantilever with sample, 6 - laser diode, 7 - PSD; c) Interferometric setup. 8 - optical fiber.

3.2 The TDESR probe

Design of the probe was based on the previous experience with TDESR probe with capacitive detection, designed by Fadi El Hallak [30]. The new probe had to be customized in order to fit into the Spectromag SM4000. To prevent vibrations caused by helium gas flow in the cryostat, an inner static exchange gas chamber was implemented.

The designed probe can be seen in Fig. 3.3 and Fig. 3.4. In Fig. 3.3 we can see a detail of the top part of the probe. For precise alignment of the sample with respect to the magnetic field, a stepper motor with a planetary gearhead (Faulhaber AM2224-V-12-75-11 with 23/1 159:1 gearhead) was used, allowing angular resolution of 0.05° (pos. 1). The motor is coupled to the sample holder rod (pos. 6), which can be slid up and down (pos. 2) to perform *in-situ* alignment of the microwave and sample holder (Fig. 3.4). To ensure connections for all the necessary equipment inside the cryostat, three feedthroughs were implemented - one permanently dedicated

to the temperature sensor (pos. 5), which has to be used for every type of measurement, and two variable feedthroughs, which may or may not be used, depending on the type of performed experiment. In Fig. 3.3 we see a version which uses one for BNC connector for control of the piezoelectric crystal (pos. 3) and one FC/PC connector for optical fiber (pos. 4). To prevent vibrations induced by the flow of helium gas an internal static exchange gas chamber has been implemented (pos. 9). Atmosphere of the chamber is controlled through one port (pos. 8). The sample holder rod, together with the optical fiber, is enclosed in a housing to separate them from the rest of the assembly (pos. 7). Metal plates (pos. 10), which serve both as temperature shields and as cable guides, are welded on the outside of the housing.

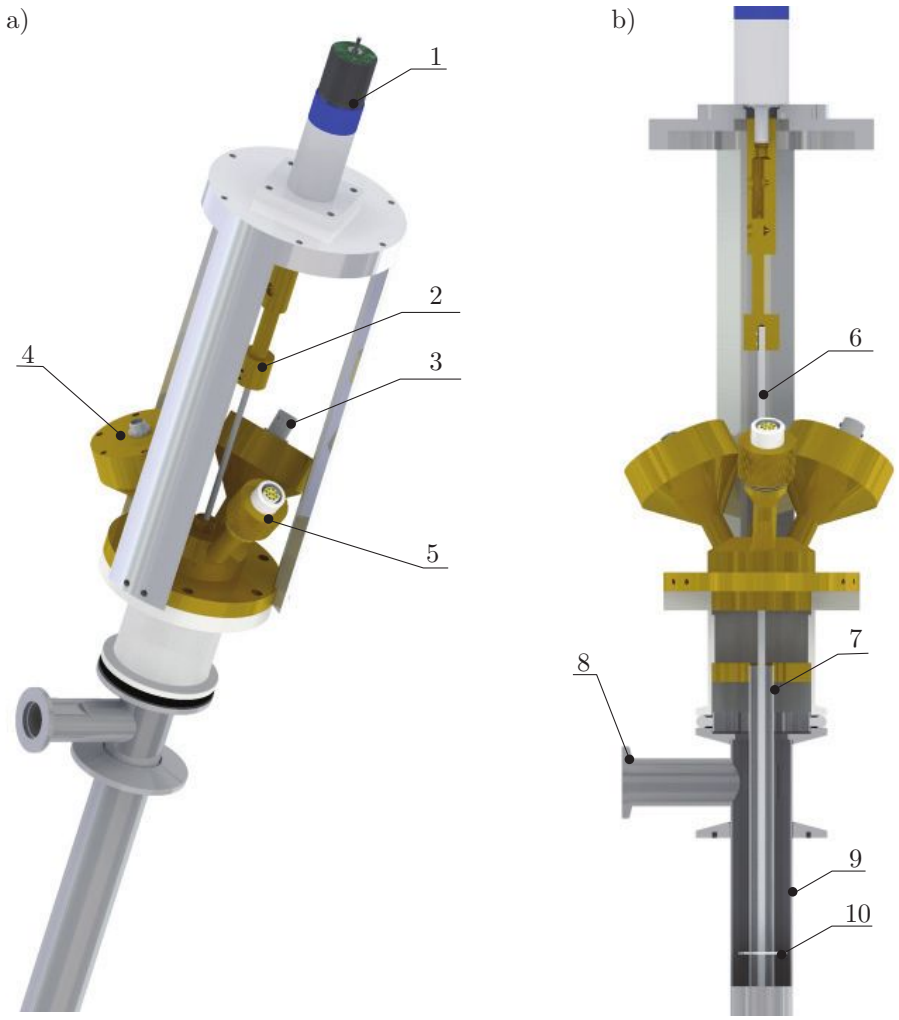

Fig. 3.3: Detail of the top part of the probe. a) 1 - stepper motor, 2 - up/down slider, 3 - BNC feedthrough, 4 - optical fiber feedthrough, 5 - temperature sensor feedthrough; b) 6 - sample holder rod, 7 - sample holder rod and optical fiber housing, 8 - internal gas chamber port, 9 - internal static exchange gas chamber, 10 - temperature shields/cable guides.

Bottom part of the probe is shown in Fig. 3.4. The sample holder rod ends with the probe head (pos. 3), which encloses the sample holder (pos. 4) with the cantilever and the studied sample (pos. 6). In order to ensure optical access to the sample holder, there are two apertures in the internal static exchange gas chamber in positions corresponding to Spectromag's windows. These apertures are covered with 125 µm thick Mylar foil, which has been glued on to the chamber with a two-component glue. The sample holder has a hole on the lower part, which allows to perform the MW alignment procedure *in-situ*, by conveniently sliding the sample holder up or down (Fig. 3.4b, c).

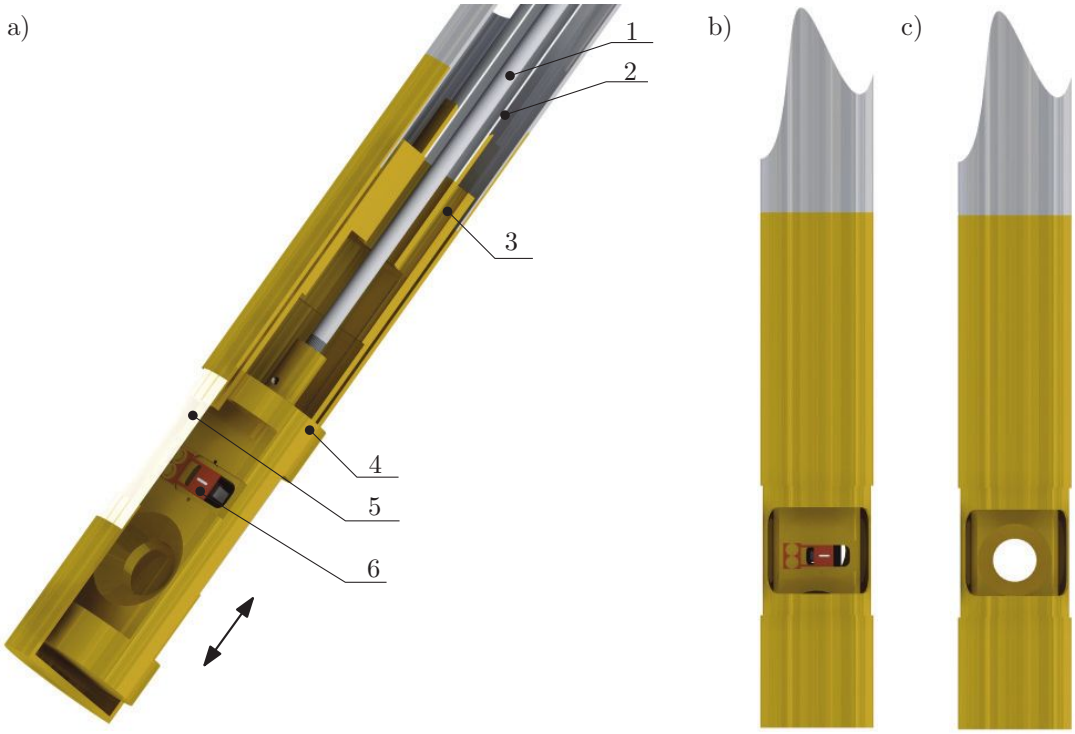

Fig. 3.4: Detail of the bottom part of the probe. a) 1 - Sample holder rod, 2 - sample holder rod and optical fiber housing, 3 - probe head with feedthroughs for cables, 4 - sample holder, 5 - Mylar foil, 6 - cantilever with sample; b) sample holder in the TDESR measurement position; c) sample holder in the position for microwave alignment.

3.2.1 Designed TDESR sample holders

Altogether three different sample holders were designed, all of them made from brass, since it is non-magnetic and has a good thermal conductivity. The first one was the same as used in the previous, capacitive detection, designed by Fadi El Hallak [30]. However, it was not used in this thesis, thus it won't be described, but can be found in the appended mechanical drawings. The second one is a slightly

modified sample holder to be used for the laser beam deflection detection, which was done by enabling optical access to the back side of the cantilever (Fig. 3.5).

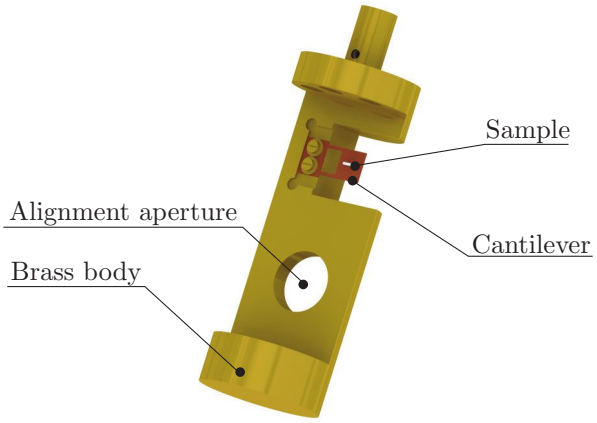

Fig. 3.5: Sample holder for laser beam deflection detection.

For the interferometric detection, a third sample holder was developed (Fig. 3.6). In order to adjust the sensitivity, the whole assembly with the piezoelectric crystal (Noliac NAC2011) and the fiber tip can moved along the cantilever sample area. With the piezoelectric crystal, the fiber tip - cantilever distance can be adjusted within 3 µm to achieve optimal working distance. All parts were manufactured by the mechanical workshop of Institute of Physical Chemistry, University of Stuttgart. Complete mechanical drawing documentation is appended to this thesis, digitally on CD as well as physically.

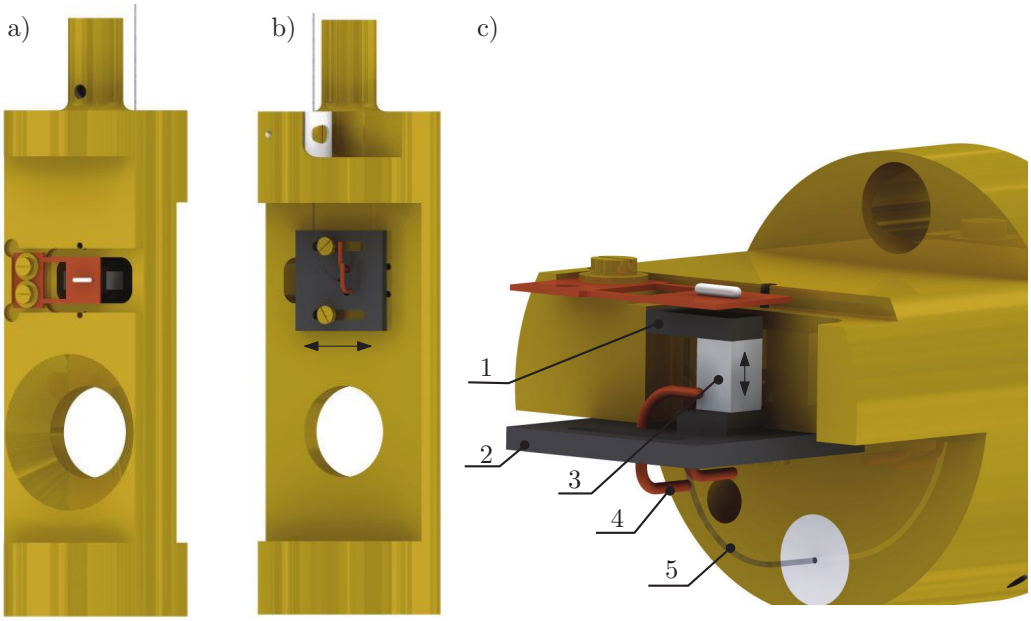

Fig. 3.6: Sample holder for interferometric detection. a) Front; b) back ; c) 1 - optical fiber tip holder, 2 - piezo stage movable along the cantilever, 3 - piezoelectric crystal, 4 - cables for piezo control, 5 - optical fiber.

3.3 Data acquisition and system control

For control of the various experimental systems, home-written LabView programs were used. The Spectromag system was controlled via the LabView program "System Program.vi", written by Dominik Bloos [46]. To visualize and save data from the PSD and control the BWO a different dedicated program was written. As mentioned earlier, output from the PSD goes through a signal processing unit with an RS232 output. It can send out data either every 2 ms or every 5 ms. This data is in the form of 12 hex numbers, each group of 4 numbers corresponding to X position, Y position and sum voltage of the PSD, respectively. This string of data is then separated, converted and scaled to millimetres and voltage (see Fig. 3.7).

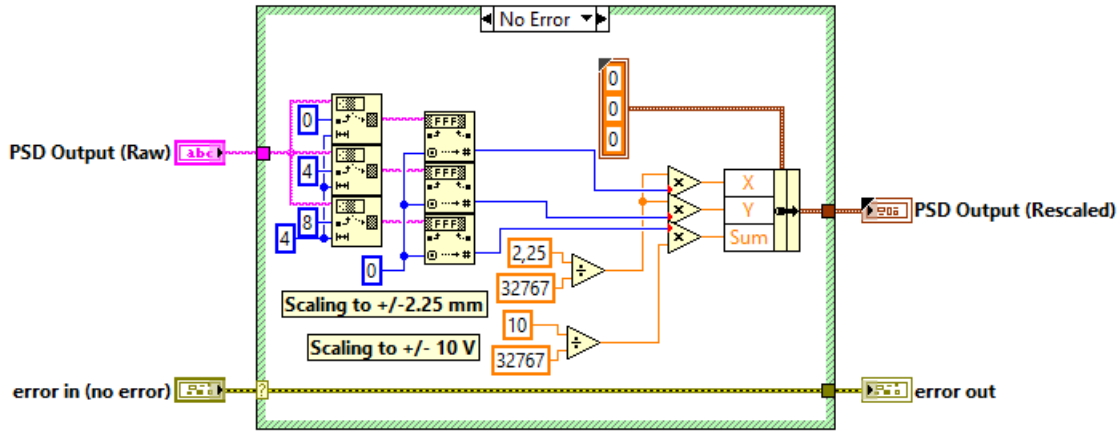

Fig. 3.7: Processing of raw data from the PSD - a 12 number hex is separated into groups of 4, converted and scaled.

A simplified diagram of the whole program can be seen in Fig. 3.8. The user has to choose the path where to save data, COM port with the signal, conversion speed set on the signal processing unit (which sets the bandwidth of RS232 communication) and the number of points to average. To obtain a reasonable amount of data, usually 100 points are averaged with 5 ms conversion speed (leading to 2 points per second).

Front panel of the virtual instrument, used during the measurement, can be seen in Fig. 3.9. Since the signal is usually seen in the X dimension of the PSD, only this value is shown in the graph (in the measurement file both X and Y signals can be found). To be able to look at the signal without saving the data (during alignment, preparations or troubleshooting), recording of the data can be switched on or off. The program also incorporates an independent subprogram for control of the BWO, which can be turned on or off. When its on, the user can either set one static frequency or perform a frequency sweep. Control of the magnetic field and

temperature is done by a separate program, however the values of magnetic field, VTI temperature and TDESR temperature are being read out and saved along the measured positional data.

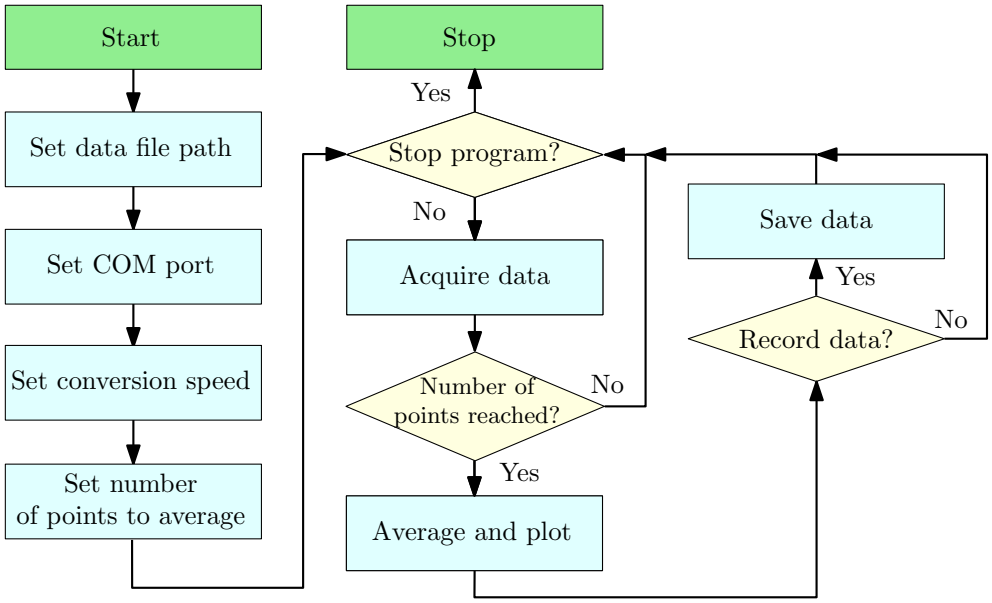

Fig. 3.8: Simplified flowchart depicting the base of PSD readout program. The BWO control part runs independently from this portion.

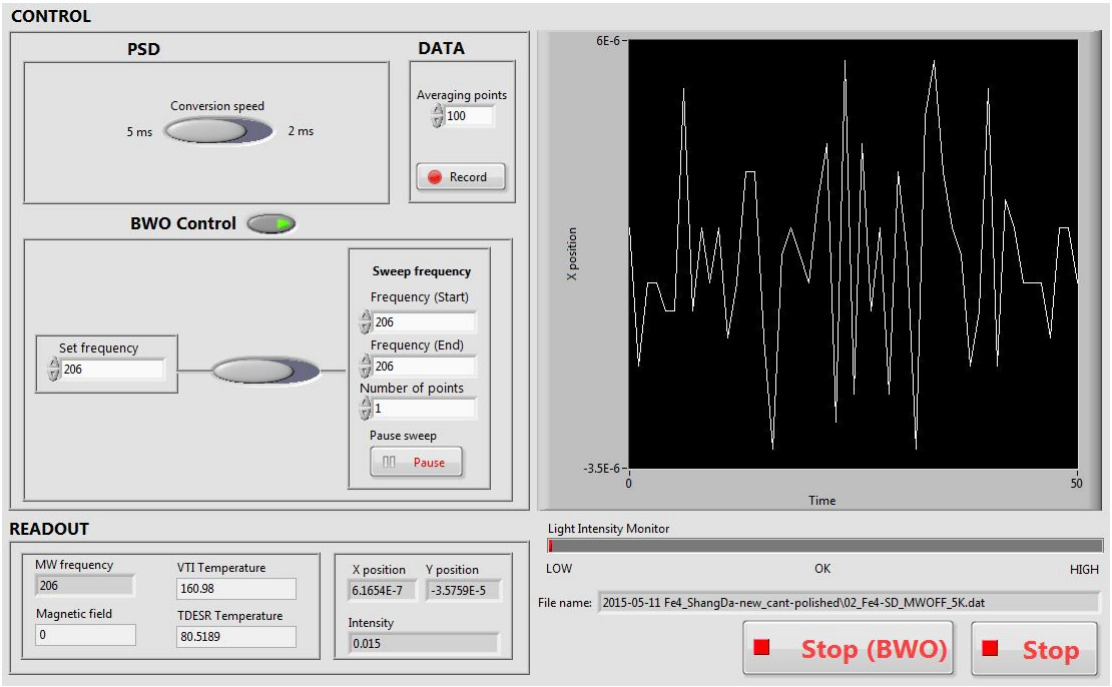

Fig. 3.9: Frontpanel of the virtual instrument used during measurements. It contains a readout of the PSD positional data and experimental conditions (magnetic field, temperature) from the Spectromag. A BWO control subprogram is also available.

4 MEASUREMENTS WITH OPTICAL DETECTION

To test the designed optical detection systems we have carried out several measurements. To proof the concept of laser beam deflection measurement of TDESR, we have first carried out bench-top room temperature cantilever torque magnetometry on ferromagnetic thin films at the Institute of Physical Engineering, Brno University of Technology. The setup was then transported to the Institute of Physical Chemistry, University of Stuttgart, where it was implemented into to the TDESR spectrometer and TDESR measurements on SMM single crystals were performed. With the interferometric setup, only bench-top system testing was performed due to a malfunction of used piezoelectric crystal.

4.1 Laser deflection detection

4.1.1 Bench-top CTM

To test the feasibility of our laser deflection setup, bench-top cantilever torque magnetometry was performed as proof-of-principle at Brno University of Technology. A schematic drawing of the experimental configuration can be seen on Fig. 4.1. Light from a He-Ne laser (wavelength 632.8 nm, 5 mW, pos. 1) is reflected from a mirror (pos. 2), focused through a lens (pos. 3) on the cantilever with sample (pos. 4, 6) and reflected onto the PSD (pos. 7). The cantilever and sample is placed in a magnetic field generated by a home-built toroidal coil attached to a rotatable holder (pos. 6). Whole setup was placed on a damped optical table to prevent external vibrations. The cantilever was the same as we used for sensitivity calculations in 2.1. The cantilever was fixed with two screws onto a damped optical post, schematically shown on Fig. 4.1b.

As the sample, we have chosen a thin strip of permalloy ($Ni_{80}Fe_{20}$) with the dimensions 10 μm×995 μm×50 nm (see Fig. 4.2). The permalloy strip was deposited on a gold rectangular waveguide on a 6 mm×5 mm silicon wafer. The waveguide was designed for a different type of experiment not described here. Patterning was done via two step electron beam lithography process and the deposition of materials with ion beam assisted deposition at room temperature.

Due to the roughness of the unpolished cantilever surface, the reflected spot was diffused over a large area (see Appendix A for more details) and the detected signal highly noisy. Nevertheless, we have obtained a proof-of-concept measurement, which can be seen in Fig. 4.3. We have simulated the data using a home-written Matlab

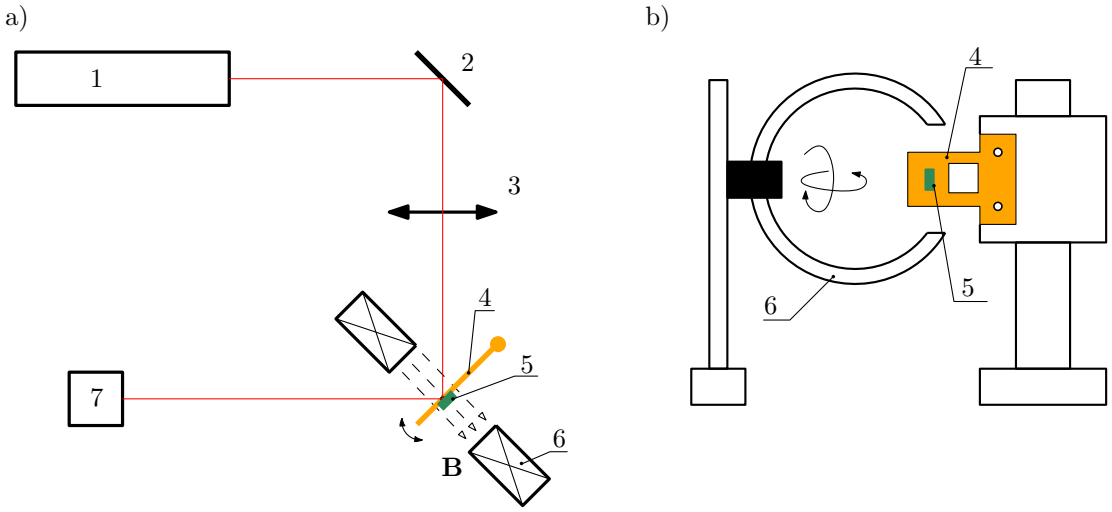

Fig. 4.1: A schematic drawing of the experimental setup. a) Top view. 1 - HeNe laser, 2 - mirror, 3 - focusing lens, 4 - cantilever, 5 - sample, 6 - rotatable toroidal coil, 7 - PSD. b) Detail of cantilever and coil.

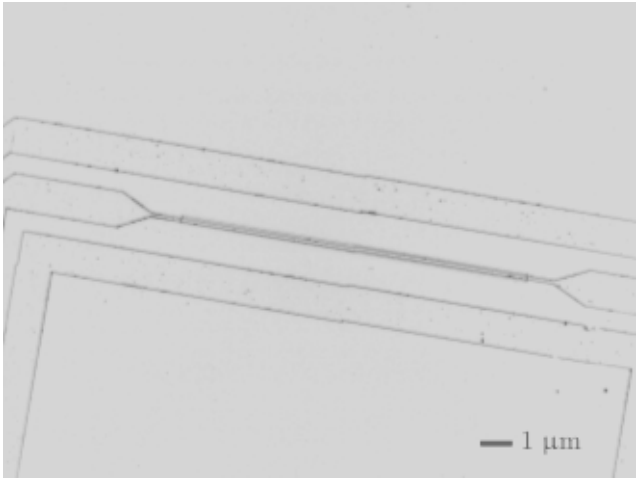

Fig. 4.2: Permalloy thin strip (10 µm x 995 µm x 50 nm), deposited on a gold waveguide in the middle. Image from an optical microscope.

program by calculating the equation $\tau_y = BM \sin\theta$, as described in section 1.3.1. Due to lack of equipment for proper magnetization measurements, we have made only qualitative simulation, in which the best fit was obtained for a saturation field of 50±2 mT. To make this method truly quantitative, we would need to measure the same sample with a different magnetometer for confirmation. We would also need to take into account additional factors, such as the influence of the amount of torque with which the screws that hold the cantilevers were screwed in, or the possible shift in the absolute values of magnetic field due to slightly different placement of the cantilever and the Hall bar used for calibration of the magnetic coil.

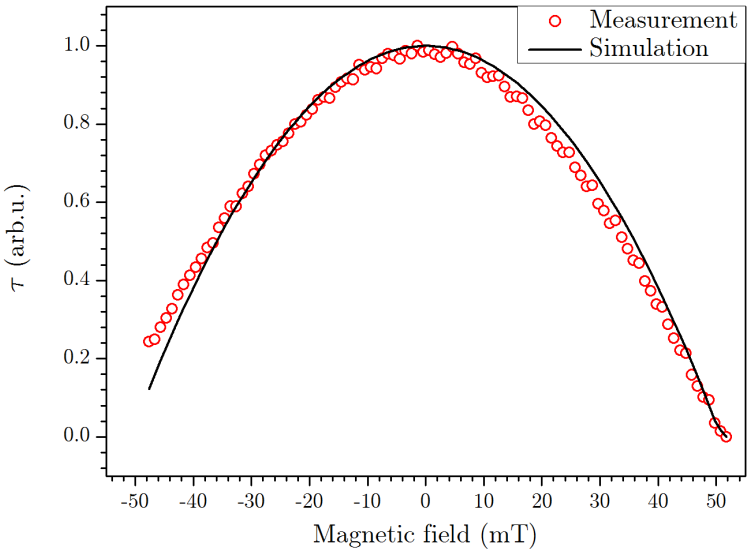

Fig. 4.3: Measurement and qualitative simulation of the magnetization of a permalloy thin strip.

4.1.2 TDESR

All test measurements of our TDESR setup were carried out on Single Molecule Magnets with known ESR spectra, to test the reliability and sensitivity of the new detection schemes using the setup described in chapter 3. For our measurements we used the Fe_4 derivative molecule with a ground state spin of $S = 5$. This compound, with the formula $[Fe_4(L)_2(dpm)_6]$, where (Hdpm) = 2,2,6,6-tetramethylheptane-3,5-dione and (H_3L) is the tripodal ligand R′-O-$CH_2C(CH_2OH)_3$ with R′=(R,S)-2-methyl-1-butyl was synthesized by the group of prof. A. Cornia [47]. The molecule is on Fig. 4.4, where also the orientation of its easy axis can be seen. We have chosen this sample due to the fact that it was previously measured by capacitive detection.

After mounting the sample on the cantilever with the crystal plane $(10\bar{1})$ lying on the cantilever (Fig. 4.4) and sample holder (Fig. 4.5), the assembly was inserted

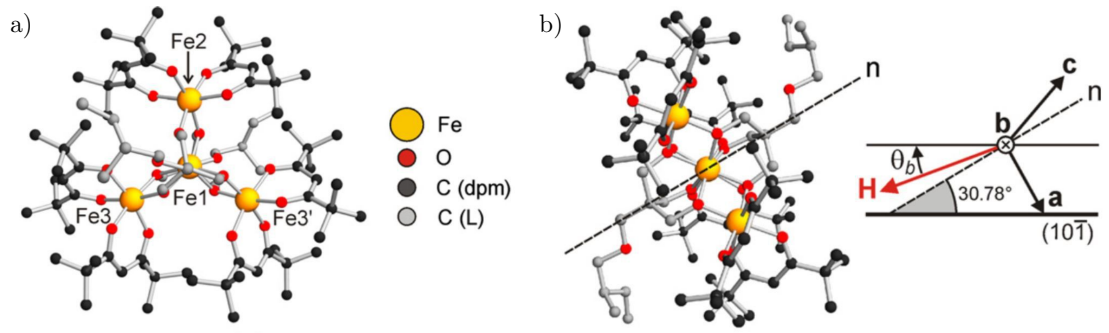

Fig. 4.4: Molecular structure of the Fe_4 SMM used for test measurements viewed a) normal to the metal plane, b) along the crystallographic **b** axis. In par b) we can see also unit cell axes **a** and **c**, along with normal to the metal plane **n**, which corresponds with the easy axis of the molecule. During measurement, the sample is lying with the (10$\bar{1}$) plane on the cantilever. Pictures taken from [48].

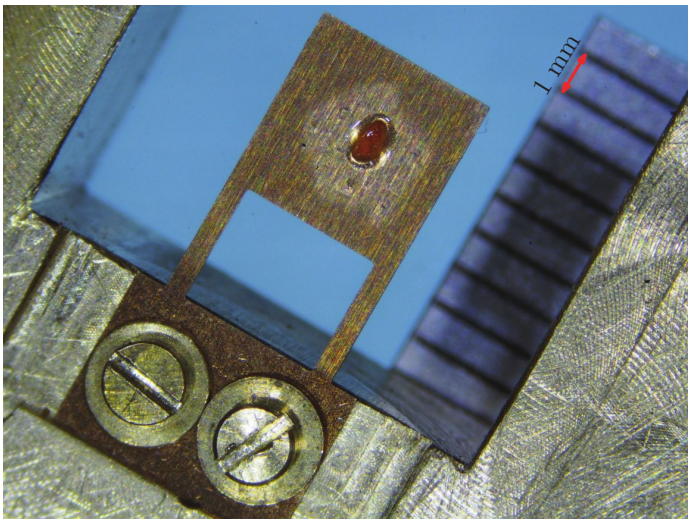

Fig. 4.5: Picture from an optical microscope of the Fe_4 single crystal mounted on the cantilever.

into the internal static exchange gas chamber and pumped to 1.6×10^{-4} mbar. The whole probe was inserted into the VTI, filled with He gas to quicken the cooling process, then cooled to 11 K and pumped again (1×10^{-5} mbar) to limit gas-flow-induced vibrations. After pumping the gas chamber was closed with a valve and the temperature was allowed to stabilize to 11 K.

The first successful measurements of TDESR measured via laser deflection detection can be seen in Fig. 4.6a. During simultaneous field sweep and MW irradiation with frequency 180 GHz we have observed a peak at approximately 2.7 T, which was an expected ESR signal [47] - after turning the MW radiation off, the peak disappeared as expected. To further prove it is indeed an ESR signal, we set the field to 4.5 T and swept the available MW frequency range from 155 GHz to 255 GHz (Fig. 4.6b), where we observed expected three resonance peaks. The peaks I, II and III correspond to transitions from $M_S = -5$ to $M_S = -4$, $M_S = -4$ to $M_S = -3$ and $M_S = -3$ to $M_S = -2$ respectively.

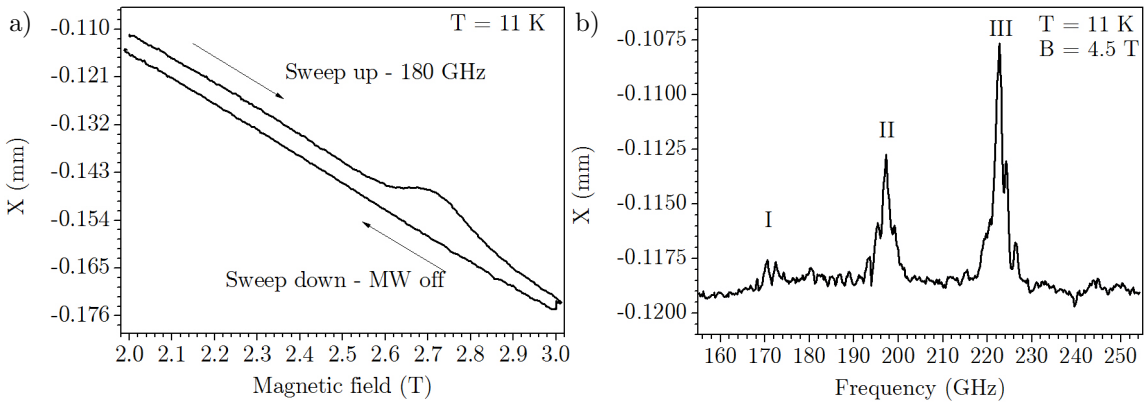

Fig. 4.6: First succesfull measurements of a) field swept TDESR, b) frequency swept TDESR on the Fe_4 SMM.

In Fig. 4.7 we can see measured temperature dependence of the signal for a single frequency of 190 GHz, along with simulation of the data. To focus solely on the ESR signal, the magnetization curve was fitted with a spline and subtracted. In the temperature dependence can be seen how at low temperatures mainly the lowest $M_S = -5$ state is populated, therefore the transition $M_S = -5$ to $M_S = -4$ is most intense. With raising the temperature the population between the states starts to spread out according to the Boltzmann distribution and we can see more peaks that are less intense. Simulation was done using the Easyspin package for Matlab [31], using anisotropy parameters determined by HFEPR given in literature [47] shown in table 4.1. We have simulated that the easy axis of the molecule has enclosed a $32° \pm 0.5°$ angle with the magnetic field - since the easy axis encloses a 30.78° with

Tab. 4.1: Parameters used in Easyspin simulations, taken from [47].

g	$D\,[\mathrm{cm}^{-1}]$	$E\,[\mathrm{cm}^{-1}]$	$10^5 B_0^4\,[\mathrm{cm}^{-1}]$
2.000	-0.449	0.030	2.400

the cantilever plane, we can say, that between the cantilever and the magnetic field was ≈1°. We have investigated the angular range in which the reflected spot could be found by slowly rotating the sample holder with the stepper motor and found out it is less than 2.5°. Since the torque signal has a maximum at 45°, the crystal has to be properly positioned *ex situ*, as a 1-2° change of angle won't affect the strength of the signal significantly. In the case of our sample, this wasn't a problem since it has a convenient easy axis orientation - in case of other samples a small metal angle on top of the cantilever has to be used in order to properly align the sample with respect to the magnetic field.

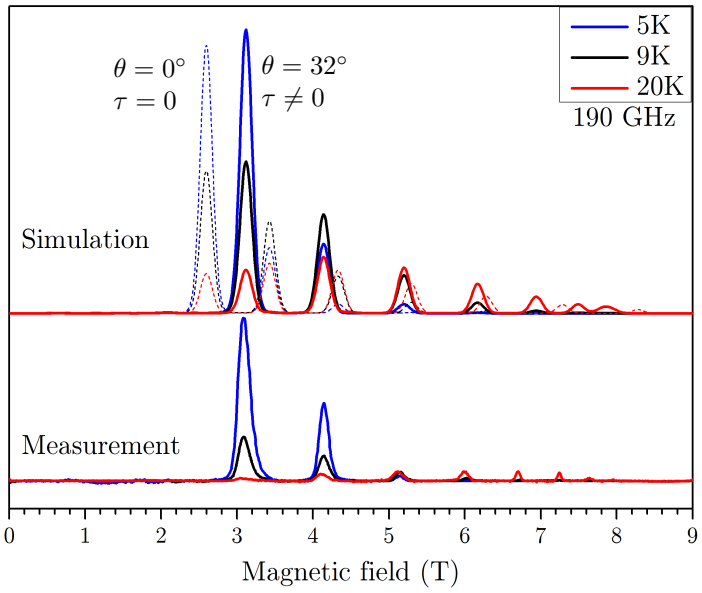

Fig. 4.7: Measured temperature dependence along with simulated data.

A number of measurements was taken to compare field and frequency sweeps which were then also compared to previous detection scheme - these measurements can be seen in Fig. 4.8 and Fig. 4.9. We can see both in Fig. 4.7 and Fig. 4.8a that with optically detected field sweeps, after subtraction of the magnetization signal, we obtain smooth, well resolved peaks with signal-to-noise as high as 36, depending on the irradiation frequency. The reason for different absolute intensities at different frequencies is the BWO output, which has very different output powers

at different frequencies (see Appendix B). With this resolution line-shape studies can be performed or hidden peaks could be noticed by resolving main peak shoulders. During field sweeps, if the magnetization signal is too strong, only a limited field range can be swept at once, as the laser spot will either leave the PSD or the window altogether. This can be to some degree compensated by changing the PSD-cantilever distance and/or using a lens, but this also affects the resolution, therefore it is another factor that need to be considered when setting up the measurement. Compared to the capacitance measurements (Fig. 4.8b), we can see that there the signal-to-noise is comparable, but the line-shape is not so satisfactory due to very slow data acquisition. A sweep from 0 to 7 T takes $\approx$ 45 minutes, whereas our spectrum can be recorded in 7 minutes with much higher number of points.

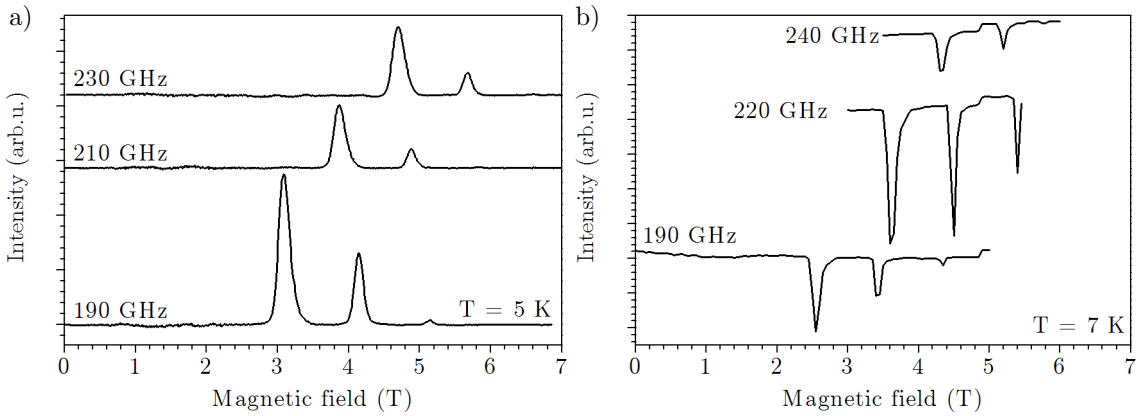

Fig. 4.8: Comparison of a) laser beam deflection, b) capacitance field sweeps. Capacitive measurements data courtesy of María Dörfel - shifts in peak positions caused by different angle between easy axis of the crystal and the magnetic field.

The frequency sweeps, seen in Fig. 4.9, have one advantage compared to the field sweeps. Since the field is kept constant, the PSD position has to be adjusted only once, after setting the required field and then the whole frequency spectrum can be recorded without laser spot leaving the active area. However, apart from that (and faster sweeps), these measurements are much more problematic, mainly due to the mentioned unstable output power of the BWO. Due to that, the spectra contain a lot of artefacts, distort line-shapes and possibly drown out useful signal, when the peak is moved to a position corresponding to a dip in the output power. The signal-to-noise is also worse, at best 11. Although a calibration curve for the output power can be obtained, a simple subtraction/division won't help - this was already tried by El Hallak in his thesis [30]. We think this can be caused by an ever present shift in the actual frequency. The BWO output frequency is controlled via voltage, but this voltage-to-frequency conversion is a polynomial and slightly differs in voltage-to-frequency and frequency-to-voltage calculations. Due to this

it is not easy to precisely correlate different measurements and a division usually results in even worse spectra. Another problem are standing waves created between the various components on the optical path, which create baseline oscillations. A solution to both of these problems could be expanding the QO setup to contain also a circulator, a non-reciprocal device which would partially eliminate standing waves. Additionally, by including the Golay cell at the circulator output, would enable us to monitor output power of the BWO directly during the measurement and eliminate power oscillations from the spectra. The capacitance measurements share the same problems with the frequency sweeps and offer comparable resolution.

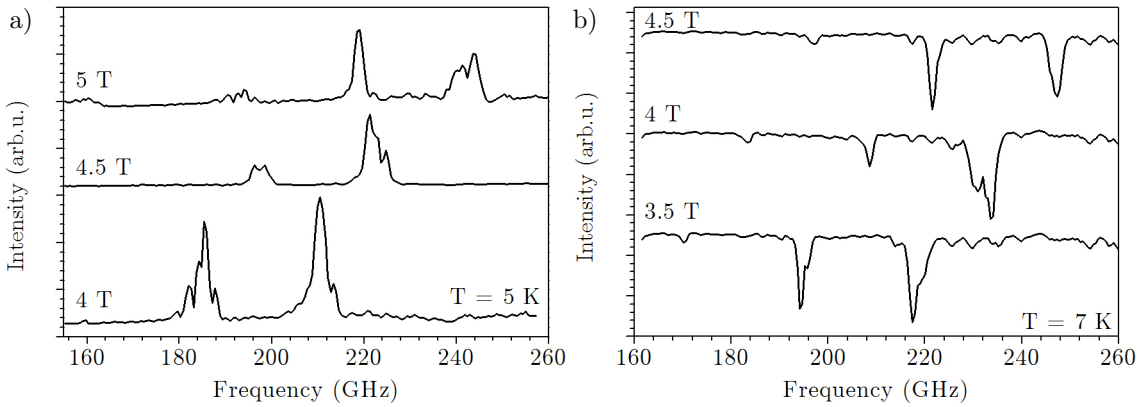

Fig. 4.9: Comparison of a) laser beam deflection, b) capacitance field sweeps. Capacitive measurements data courtesy of María Dörfel - shifts in peak positions caused by different angle between easy axis of the crystal and the magnetic field.

To conclude the comparison, laser beam deflection in its basic form has proven itself to offer better results than capacitive detection scheme (which already uses lock-in), with the advantage of faster scans, higher resolution, resistance to electrical noise and requirement of no additional components in the magnet. There are, however, some disadvantages to consider: limited angular range, limited range of magnetic fields accessible in one measurement in case of samples with strong magnetization signal and the need of highly polished cantilevers.

In terms of further development of the detection scheme, currently the weakest part is the laser diode. It has an elliptical beam output which in itself wouldn't pose a problem, but although in the product description is written that obtaining a collimated beam is possible with the integrated lens, the reality is quite different. It could be possible to improve the measurements by removing the integrated lens and constructing a simple collimator from a circular aperture and a lens. The collimated circular beam could then be used directly, or further manipulated - decreasing of the spot diameter or focused with a normal lens. However, due to the low power output (4.5 mW), it is possible that not enough light intensity would be reflected

back to the PSD. Used laser diode also has no power stabilization, it is therefore possible that power fluctuations of the laser power output might be seen on the detector as an additional noise component - however, we don't have the necessary equipment to prove or disprove this assumption. Another option to consider, for both field and frequency sweeps, is the implementation of the lock-in technique, described in section 1.4. To implement field modulation, a small coil would have to be included in the sample holder - this would require very careful considerations in terms of design, since the limiting outer dimension in the sample holder space is a 19.9 mm diameter. Another limitation is the detection bandwidth - modulation frequency commonly used in ESR spectrometers is 100 kHz. Our signal processing unit, however, allows digital signal readout only in two modes - every 5 ms (200 Hz) or 2 ms (500 Hz). Although lock-in even at these frequencies would definitely benefit the measurements, the restriction to 2 frequencies is quite limiting. A workaround to this is available - the unit offers also an analog output, although with one order of magnitude worse resolution. It is, however, quite possible that this drop in resolution would be compensated by implementation of the lock-in.

4.2 Interferometric detection

Initial assembly and testing of the interferometer was done by Dalibor Šulc at the Institute of Physical Engineering in Brno - later he transported the assembly to the Institute of Physical Chemistry in Stuttgart. In the initial testing, we have used the setup described in section 2.2, only instead of the cantilever we have used a regular mirror mounted on a piezoelectric tube scanner. (Fig. 4.10). Whole setup was placed on an optical table.

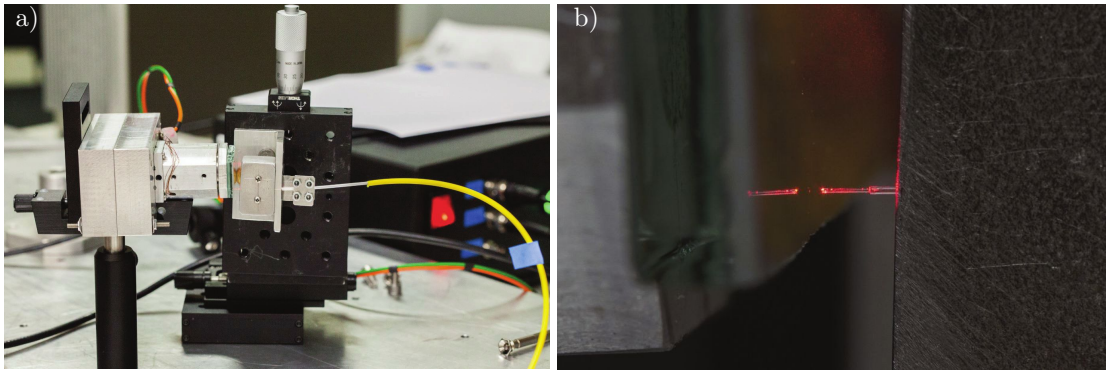

Fig. 4.10: Pictures of the interferometric testing setup. a) Fiber holder with fine adjustment screws and a mirror mounted on a piezoelectric tube scanner, b) closeup on the fiber tip.

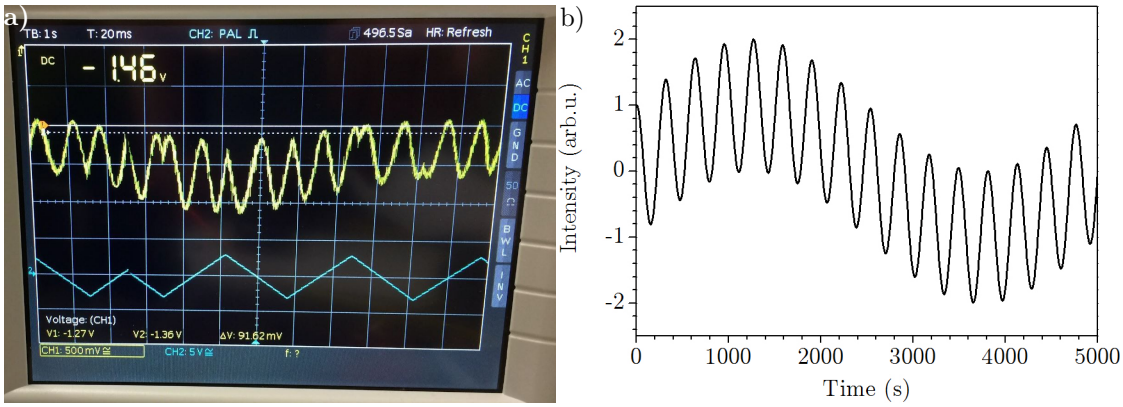

Fig. 4.11: a) A photograph capturing the measurement on an oscilloscope. Yellow line is the measured signal. Blue signal is the piezo control voltage. b) A simulation of the slow intensity mean value oscillation due to fluctuations of laser intensity.

After assembly, a triangular signal was sent to the piezo to move it back and forth and the expected sinusoid was measured (yellow signal in Fig. 4.11a). We can observe two types of noise in the measured signal. Relatively small, fast noise caused probably by vibrations and the laser instability is distorting the sinusoid, but the signal is still distinguishable. Noticeable is also a slow oscillation of the mean value, which eventually caused periodical saturation of the photodiode. We have measured the long-term stability of the HeNe laser by using the reference photodiode and, as can be seen in Fig. 4.12, this particular laser has proved unsuitable for our purposes. Although we can see that the Root-Mean-Square (RMS) noise of the laser decreases after warming up, it doesn't converge to a stable value - on the contrary, after $\approx$ 12 hours it starts rising again. Interesting is that we haven't observed the slow oscillation, noticeable in the interferometric measurements - they have been most probably averaged out.

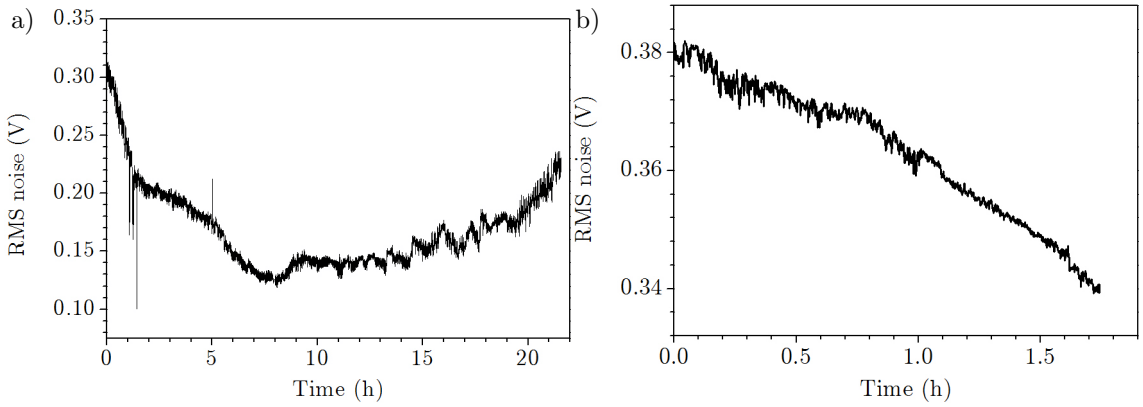

Fig. 4.12: Power stability measurements of a) HeNe laser and b) laser diode.

To further investigate this issue, we have tried replacing the HeNe laser with our laser diode from deflection measurements. As expected, since it also doesn't have any form of stabilization, the smaller noise is much worse than with the gas tube (Fig. 4.13). However, the slow drift wasn't observable when using the diode. Further testing would be necessary to definitely prove it, although it was easily simulated that drift could be caused by periodical fluctuations of intensity(Fig. 4.11b).

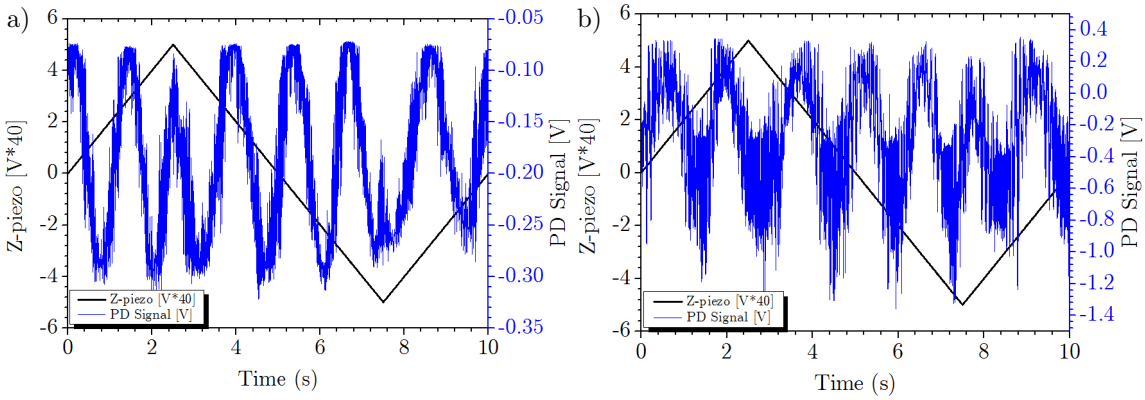

Fig. 4.13: Comparative measurements with a) HeNe laser and b) lase diode as the laser source. We can see that the laser diode gives much worse signal.

Another thing we noticed was relatively high background light intensity on the photodiode, most probably due to reflections at fiber-fiber connections, which lifted the signal close to saturation and could be another reason for worse resolution. As at the interference minimum the signal was not zero, it decreased the number of resolvable light levels. This could be caused by usage of FC/PC connectors, which have straight edges at the end - FC/APC connectors should be used instead, since they have a slight (8°) angle at the end, ensuring that the scattered light doesn't fulfil the total reflection condition.

We have then proceeded to assemble the interferometric sample holder together with the optical fiber and cantilever (Fig. 4.14). After gluing all the parts together with low temperature varnish and putting voltage on the piezo in order to start testing, the crystal has been burned - it was most probably a faulty piece. A new one didn't arrive in time to proceed with the tests and therefore more data couldn't been obtained.

Nevertheless, we have identified multiple issues in the setup which can be already addressed. We have established that a stabilized light source is crucial - most suitable would be a pigtailed (to avoid problems with coupling the laser into the fiber) so called "butterfly" laser diode, which can be, with a correct driver, stabilized not only in terms of power and wavelength, but also thermally. Important point is replacement of FC/PC connectors for FC/APC and also decreasing the number

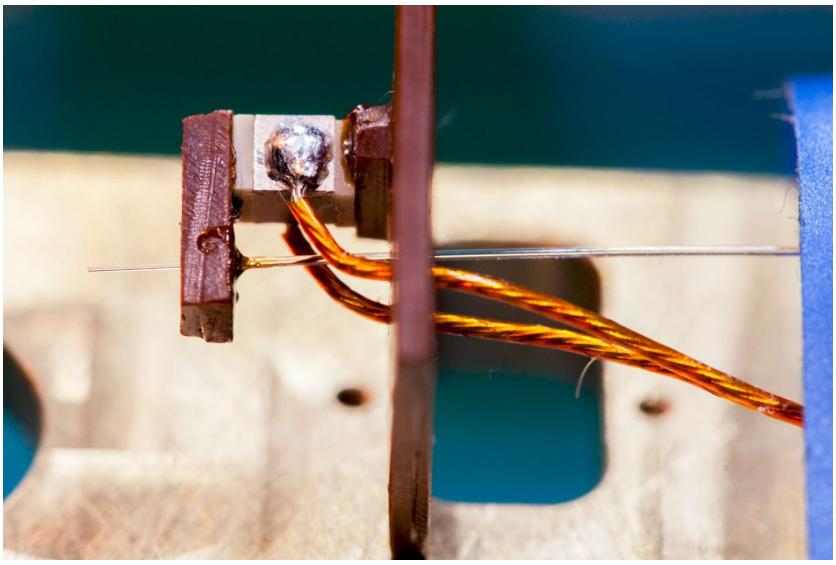

Fig. 4.14: A picture of the interferometric sample holder assembly. We can see there the piezoelectric crystal glued to the movable platform from one side and the fiber tip holder from the other. All parts are glued togehter with low temperature varnish.

of used connectors, for example by attaching the optocoupler directly to the photodiodes. We have also noticed that a preamplifier with variable gain would be highly practical, to adjust the readout levels as needed to avoid saturation of the signal without the need to resolder various components. Even though the optical fiber we have used (Thorlabs 630HP) has in its datasheet a note about enduring tight bend radii, but in reality to bend it enough for fitting onto the sample without breaking has proved to be challenging. Bend insensitive fibers (such as Thorlabs CCC1310-J9) would be more suitable for our purposes.

Another simpler, but more expensive option, would be to buy a whole setup in one package. For our purposes, accustomed to vacuum and low temperature purposes, is the Attocube FPS1010 together with microoptics at the fiber tip, enabling greater distance from the cantilever, claiming a 25 pm resolution. This system, together with all necessary accessories, costs altogether €27 417.60 which is more than 4 times the custom-built-system. It would, however, save a considerable amount of time spent by assembling and programming acquisition software. Other companies offer similar systems, but quotations were not obtained.

SUMMARY

This work has been devoted to the improvement of the TDESR spectrometer at the Institute of Physical Chemistry, University of Stuttgart by replacing the current capacitive detection of cantilever deflection with optical methods. The laser beam deflection setup was successfully designed, manufactured, assembled and tested by measuring high quality TDESR spectra of an SMM single crystal (Fig. 4.8, Fig. 4.9). We have tested both field and frequency sweeps, identified their limits and proposed possible solutions. We have shown that this method, especially with field sweeps, provides spectra of higher quality than the capacitive measurements, enabling the user to possibly extract more information with higher certainty. The only disadvantage compared to previous detection method is the limited angular range of 2.5° in which measurements can be performed, compared to full 360° rotation of the capacitive detection. Important to note is that we believe we are not yet taking advantage of the full potential of this method. Implementation of a lock-in could significantly improve the signal-to-noise ratio. Another step would be usage of a stabilized laser source, along with optimization of the optical scheme before the cantilever.

During our work, we went over the formal assignment and designed also a setup for interferometric detection of the cantilever deflection. Even though we didn't succeed in testing the interferometric assembly completely due to the malfunction of our piezoelectric crystal, we have identified multiple issues to consider with the interferometer and offered possible solutions. Usage of the interferometric setup would have the benefit of being compactly fitted into the probe, therefore again enabling full rotation and potentially offering better resolution - at the same time requiring to measure only samples with signals much weaker than the ones currently used. To build and implement such a system would, however, require considerable resources and development, in terms of mechanical, electrical and software design. A different solution would be to buy a fully developed commercial interferometric system, where to costs can be from 2 to 4 times higher than in a custom built system.

Due to the success of our design, the laser beam deflection method is already in use for measurement of new molecular magnets. We have shown that optical methods are the correct way to continue improving the TDESR spectrometer, and with further development, it can be used for measuring perspective samples which are currently out of reach due to sensitivity, such as thin films of molecular magnets or topological insulators.

BIBLIOGRAPHY

[1] Walther Gerlach and Otto Stern. Das magnetische Moment des Silberatoms. *Zeitschrift für Physik*, 9:353–355, 1922.

[2] Gareth R. Eaton, Sandra S. Eaton, and Kev M. Salikhov. *Foundations of Modern EPR*. World Scientific, 1998.

[3] Nataliya Evgenevna Zavoiskaya. 95th Birthday of Evgeny K. Zavoisky. *EPR Newsletter*, 13(1-2), 2003.

[4] John A. Weil and James jR. Bolton. *Electron Paramagnetic Resonance: Elementary Theory and Practical Applications*. Wiley, 2 edition, 2007.

[5] Petr Neugebauer. *Development of a Heterodyne High Field / High Frequency Electron Paramagnetic Resonance Spectrometer at 285 GHz*. PhD thesis, University of Grenoble, 2010.

[6] W. Bryan Lynch, Keith A. Earle, and Jack H. Freed. 1-mm wave ESR spectrometer. *Review of Scientific Instruments*, 59:1345–1351, 1988.

[7] F. Muller, M. A. Hopkins, N. Coron, M. Grynberg, L. C. Brunel, and G. Martinez. A high magnetic field EPR spectrometer. *Review of Scientific Instruments*, 60:3681–3684, 1989.

[8] Joshua Telser, Joris van Slageren, Suriyakan Vongtragool, Martin Dressel, William M. Reiff, S. A. Zvyagin, Andrew Ozarowski, and J. Krzystek. High-frequency/high-field EPR spectroscopy of the high-spin ferrous ion in hexaaqua complexes. *Magnetic Resonance in Chemistry*, 43:130–139, 2005.

[9] H. Ohta, S. Okubo, E. Ohmichi, T. Sakurai, W.-M. Zhang, and T. Shimokawa. Developments of Multi-extreme High Field ESR in Kobe. *Journal of Low Temperature Physics*, 170(5-6):511–519, 2013.

[10] G. M. Smith, J. C. G. Lesurf, R. H. Mitchell, and P. C. Riedi. Quasi-optical cw mm-wave electron spin resonance spectrometer. *Review of Scientific Instruments*, 69(1998):3924–3937, 1998.

[11] E. Hahn. Spin Echoes. *Physical Review*, 80(1946):580–594, 1950.

[12] Ygal Twig, Ekaterina Dikarov, Wayne D. Hutchison, and Aharon Blank. Note: High sensitivity pulsed electron spin resonance spectroscopy with induction detection. *Review of Scientific Instruments*, 82(2011), 2011.

[13] M. Xiao, I. Martin, E. Yablonovitch, and H. W. Jiang. Electrical detection of the spin resonance of a single electron in a silicon field-effect transistor. *Nature*, 430(July):435–439, 2004.

[14] D. Rugar, R. Budakian, H. J. Mamin, and B. W. Chui. Single spin detection by magnetic resonance force microscopy. *Nature*, 430:329–332, 2004.

[15] D. Rugar, C. S. Yannoni, and J. A. Sidles. Mechanical detection of magnetic resonance. *Nature*, 360:563–566, 1992.

[16] H. Ohta, M. Kimata, S. Okubo, E. Ohmichi, and T. Osada. Highly sensitive detection of pulsed field ESR using a cantilever at low temperature. *AIP Conference Proceedings*, 850:1643–1644, 2006.

[17] E. Ohmichi, N. Mizuno, M. Kimata, and H. Ohta. Magnetic detection of high-resolution electron spin resonance using a microcantilever in the millimeter-wave region up to 240 GHz. *Review of Scientific Instruments*, 103903(79), 2008.

[18] Hitoshi Ohta and Eiji Ohmichi. Recent Advances in High-Frequency Electron Spin Resonance Detection Using a Microcantilever. *Applied Magnetic Resonance*, 37:881–891, 2010.

[19] Fadi El Hallak, Joris van Slageren, and Martin Dressel. Torque detected broad band electron spin resonance. *Review of Scientific Instruments*, 095105:1–6, 2010.

[20] G.A. Candela. Influence of Paramagnetic Resonance on the Static Susceptibility. Spin—Lattice Relaxation Time of Cupric Sulfate Pentahydrate. *The Journal of Chemical Physics*, 113, 1965.

[21] George A. Candela and R.E Mundy. Absolute Magnetic Susceptibilities by the Gouy and the Thorpe-Senftle Methods *. *IRE Transactions on Instrumentation*, pages 106–109, 1962.

[22] Brant Cage, Stephen E. Russek, David Zipse, and Naresh S. Dalal. Advantages of superconducting quantum interference device-detected magnetic resonance over conventional high-frequency electron paramagnetic resonance for characterization of nanomagnetic materials. *Journal of Applied Physics*, 97(2005):15–18, 2005.

[23] W. Wernsdorfer, A. Müller, D. Mailly, and B. Barbara. Resonant photon absorption in the low spin molecule V15. *Europhysics Letters*, 861:7, 2004.

[24] K. Petukhov, S. Bahr, W. Wernsdorfer, A. L. Barra, and V. Mosser. Magnetization dynamics in the single-molecule magnet Fe8 under pulsed microwave irradiation. *Physical Review B - Condensed Matter and Materials Physics*, 75:1–12, 2007.

[25] R. F. Penoyer. Automatic Torque Balance for Magnetic Anisotropy Measurements. *Review of Scientific Instruments*, 711(30):5–9, 1959.

[26] R. Griessen. A capacitance torquemeter for de Haas-van Alphen measurements. *Cryogenics*, 13(6):375–377, 1973.

[27] R. D. Biggar and J. M. Parpia. High-Q oscillator torque magnetometer. *Review of Scientific Instruments*, 69(1998):3558–3562, 1998.

[28] M. Weber, R. Koch, and K. Rieder. UHV Cantilever Beam Technique for Quantitative Measurements of Magnetization, Magnetostriction, and Intrinsic Stress of Ultrathin Magnetic Films. *Physical Review Letters*, 73(8):1166–1169, 1994.

[29] Andrea Cornia, Dante Gatteschi, and Roberta Sessoli. New experimental techniques for magnetic anisotropy in molecular materials. *Coordination Chemistry Reviews*, 221:573–604, 2001.

[30] Fadi El Hallak. *Magnetic anisotropy of molecular nanomagnets.* PhD thesis, University of Stuttgart, 2009.

[31] Stefan Stoll and Arthur Schweiger. EasySpin, a comprehensive software package for spectral simulation and analysis in EPR. *Journal of Magnetic Resonance*, 178:42–55, 2006.

[32] Dante Gatteschi, Roberta Sessoli, and Andrea Cornia. Single-molecule magnets based on iron(iii) oxo clusters. *Chemical Communications*, (9):725–732, 2000.

[33] L. Thomas, F. Lionti, R. Ballou, D. Gatteschi, R. Sessoli, and B. Barbara. Macroscopic quantum tunnelling of magnetization in a single crystal of nanomagnets. *Nature*, 383:145, 1996.

[34] J. van Slageren, S. Vongtragool, B. Gorshunov, A. Mukhin, and M. Dressel. Frequency-domain magnetic-resonance spectroscopic investigations of the magnetization dynamics in Mn12Ac single crystals. *Physical Review B*, 79:1–12, 2009.

[35] Cambridge Structural Database, 2015.

[36] G. Binnig and C. F. Quate. Atomic Force Microscope. *Physical Review Letters*, 56(9):930–933, 1986.

[37] G. M. McClelland, R. Erlandsson, and S. Chiang. Atomic Force Microscopy: General Principles and a New Implementation. *Review of Progress in Quantitative Nondestractive Evaluation*, 6B:1307–1314, 1987.

[38] Gerhard Meyer and Nabil M. Amer. Novel optical approach to atomic force microscopy. *Applied Physics Letters*, 53(12):1045–1047, 1988.

[39] Adjustable focus laser diode kit S2011-EC manual. `http://www.thorlabs.de/thorcat/5400/S2011-EC-Manual.pdf`, 2015.

[40] PSD module C10443-01. `http://www.hamamatsu.com/jp/en/C10443-01.html`, 2015.

[41] Signal processing unit C10460. `http://www.hamamatsu.com/jp/en/product/category/3100/4010/4164/C10460/index.html`, 2015.

[42] D. Rugar, H. J. Mamin, and P. Guethner. Improved fiber-optic interferometer for atomic force microscopy. *Applied Physics Letters*, 55(25):2588–2590, 1989.

[43] Thorlabs Web Catalogue. 2015.

[44] R. C. Hibbeler. *Mechanics of materials*. Pearson Education Ltd., 2003.

[45] Goodfellow, GmbH catalogue. `http://www.goodfellow.com/catalogue/GFCat4J.php?ewd_token=f66ApWT2WdhensIWahXWkf1yMwtD2m&n=bJQvXUBVVQdoZmbout3VN5jNpCUP0C`, 2015.

[46] Dominik Bloos. Improvement of the High Frequency Electron Spin Resonance Spectrometer in Stuttgart. Master's thesis, 2014.

[47] Luisa Gregoli, Chiara Danieli, Anne Laure Barra, Petr Neugebauer, Giovanna Pellegrino, Giordano Poneti, Roberta Sessoli, and Andrea Cornia. Magnetostructural correlations in tetrairon(III) single-molecule magnets. *Chemistry - A European Journal*, 15(26):6456–6467, 2009.

[48] Fadi El Hallak, Petr Neugebauer, Anne-laure Barra, Joris van Slageren, Martin Dressel, and Andrea Cornia. Torque-detected ESR of a tetrairon (III) single molecule magnet. *Journal of Magnetic Resonance*, 223:55–60, 2012.

A CANTILEVER CHARACTERIZATION

A collection of various measurements done on the CuBe cantilevers, both polished and non-polished

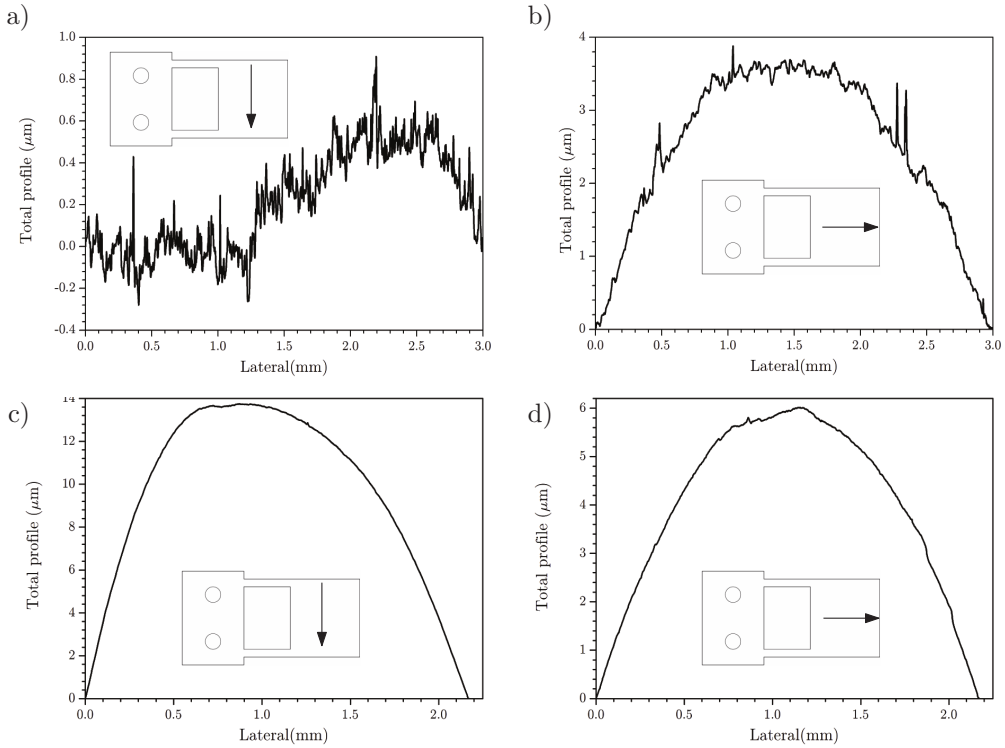

Fig. A1: Profilometry of cantilevers measured along drawn arrows: a) and b) unpolished, c) and d) polished. The parabolic shape is due to bending of the cantilevers, since for profilometry damaged cantilevers were used. Courtesy of Dalibor Šulc.

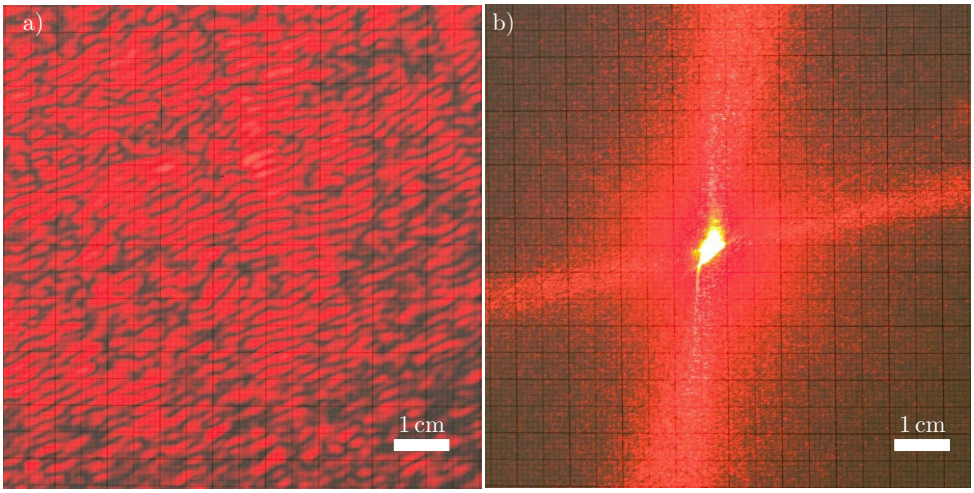

Fig. A2: Reflected spots from a) unpolished and b) polished cantilever for comparison.

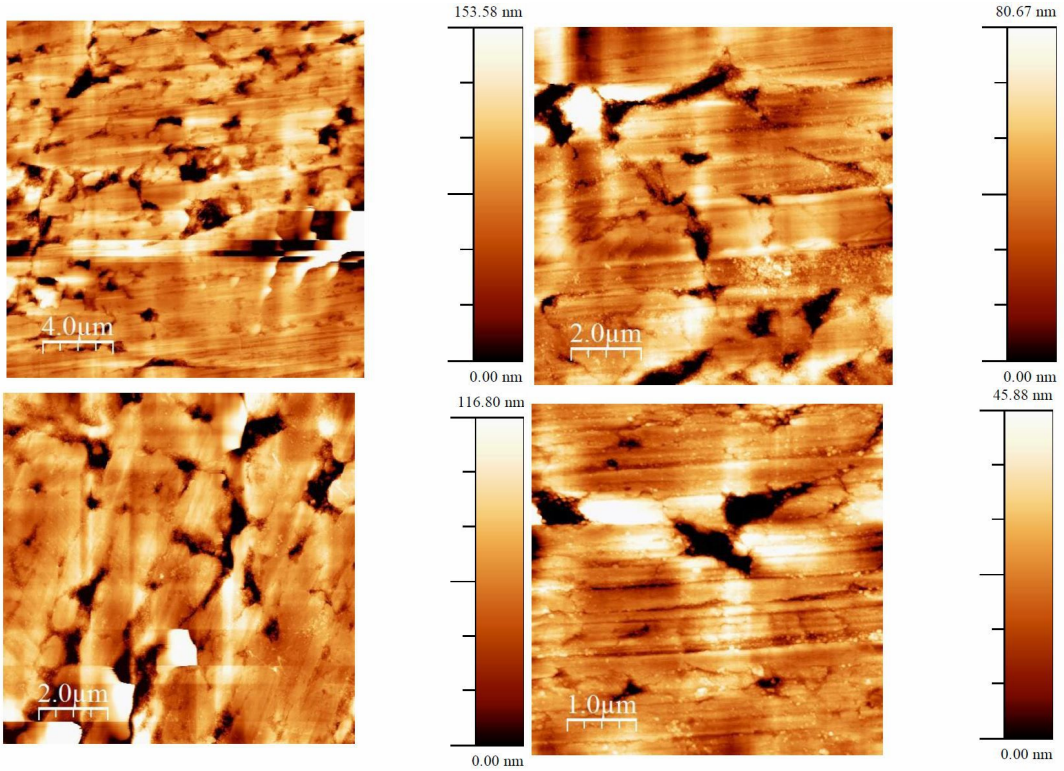

Fig. A3: AFM images of the unpolished CuBe cantilevers. RMS roughness ≈30 nm calculated from 10×10 µm images. Courtesy of PD Dr. Benedetta Casu and Dr. Francesca Ciccullo from University of Tübingen.

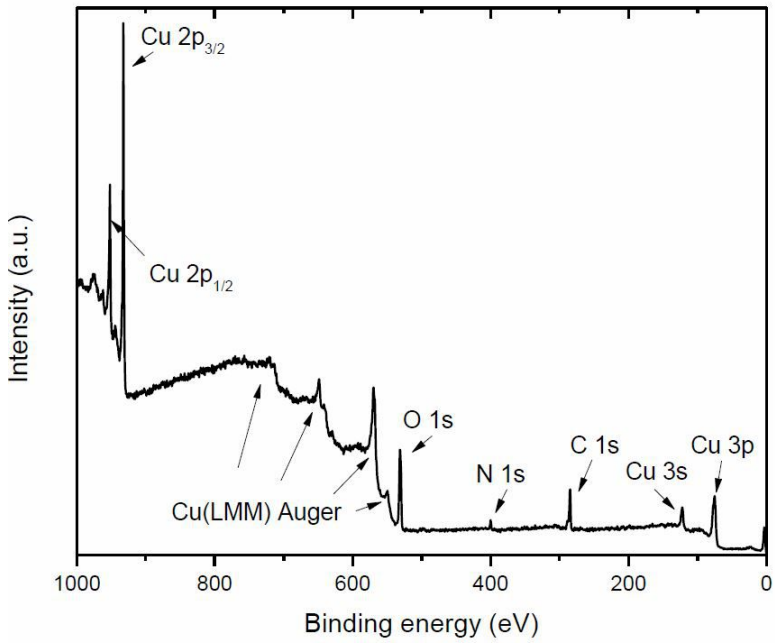

Fig. A4: X-ray photoelectron spectrum of the unpolished CuBe cantilever. Courtesy of PD Dr. Benedetta Casu and Dr. Francesca Ciccullo from University of Tübingen.

B BWO OUTPUT POWER DEPENDENCE

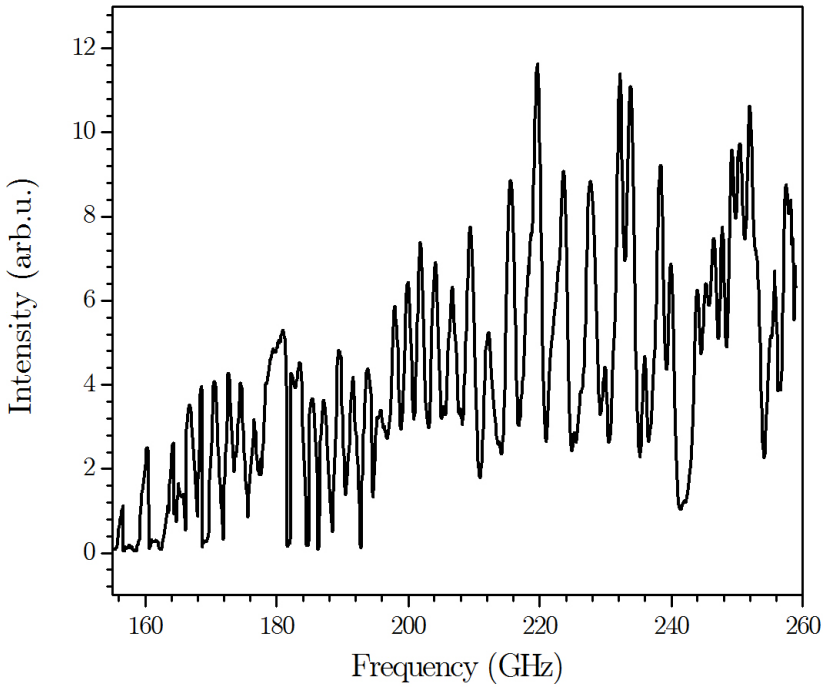

Fig. B1: Measured output power of BWO as a function of output frequency.

C LIST OF PHYSICAL APPENDICES

Attached CD

Contents:

- DP_Kern.pdf - electronic version of this thesis
- Drawings.zip - electronic version of mechanical drawings

Mechanical drawings